

Revisiting Seismic Energy of Shallow Tremors: Amplifications due to Site and Propagation Path Effects Near the Nankai Trough

Shunsuke Takemura¹, Kentaro Emoto², and Suguru Yabe³

¹ Earthquake Research Institute, the University of Tokyo, 1-1-1 Yayoi, Bunkyo-ku, Tokyo 113-0032, Japan

² Geophysics, Graduate School of Science, Tohoku University, 6-3, Aramaki-aza-aoba, Aoba-ku, Sendai 980-8578, Japan

³ Geological Survey of Japan, National Institute of Advanced Industrial Science and Technology, Tsukuba Central 7, 1-1-1 Higashi, Tsukuba, Ibaraki 305-8567, Japan

Corresponding author: Shunsuke Takemura (shunsuke@eri.u-tokyo.ac.jp)

Key Points:

- Effects of path and site on the seismic energy estimation of slow earthquakes at shallow plate boundaries were investigated.
- The assumption of far-field body waves without thick sediments causes an overestimation of seismic energies for shallow tremors.
- Scaled energies of seismic slow earthquakes at both shallow and large depths range from 10^{-10} to 10^{-9} .

Abstract

We investigated the effects of the propagation path and site amplification of shallow tremors along the Nankai Trough. Using far-field *S*-wave propagation from intraslab earthquake data, the amplification factors at the DONET stations were 5–40 times against an inland outcrop rock site. Thick (~5 km) sedimentary layers with V_S of 0.6–2 km/s beneath DONET stations have been confirmed by seismological studies. To investigate the effects of thick sedimentary layers, we synthesized seismograms of shallow tremors and intraslab earthquakes at seafloor stations. The ratios of the maximum amplitudes from the synthetic intraslab seismograms between models with and without thick sedimentary layers were 1–2. This means that the estimated large amplifications are primarily controlled by thin lower-velocity (< 0.6 km/s) sediments just below the stations. Conversely, at near-source (≤ 20 km) distances, 1-order amplifications of seismic energies for a shallow tremor source can occur due to thick sedimentary layers. Multiple *S*-wave reflections between the seafloor and plate interface are contaminated in tremor envelopes; consequently, seismic energy and duration are overestimated. If a shallow tremor occurs within underthrust sediments, the overestimation becomes stronger because of the invalid rigidity assumptions around the source region. After 1-order corrections of seismic energies of shallow tremors along the Nankai Trough, the scaled energies of seismic slow earthquakes were 10^{-10} – 10^{-9} irrespective of the region and source depth. Hence, the physical mechanisms governing seismic slow earthquakes can be the same, irrespective of the region and source depth.

Plain Language Summary

The deployment of campaigns and permanent ocean bottom seismometers (OBSs) has enabled us to investigate the activity and physical properties of offshore seismic phenomena. Our knowledge of offshore subsurface structures is still limited; consequently, many studies have used conventional analysis methods with the simplest assumptions. Using observed and synthetic seismograms near the Nankai Trough, we found a limitation in the conventional analysis method applied to OBS data. Thick sedimentary layers, which have been confirmed by seismological studies along the Nankai Trough just below the OBSs, cause an approximately 1-order overestimation of source parameters for seismic phenomena occurring around the shallow plate boundary. This overestimation may have occurred during the seismic energy estimation of shallow slow earthquakes in Hikurangi, Costa Rica, and Mexico. After correcting for the effects of thick sedimentary layers, we found that the scaled energies of seismic slow earthquakes were 10^{-10} – 10^{-9} irrespective of the region and source depth. This suggests that the physical mechanisms governing seismic slow earthquakes can be the same, regardless of region and source depth.

1 Introduction

Slow earthquakes, which are intermediate slip modes between ordinary (fast) earthquakes and stable sliding, are often observed around megathrust zones worldwide (Obara & Kato, 2016). Ordinary and slow earthquakes are distributed separately along plate boundaries (e.g., Dixon et al., 2014; Nishikawa et al., 2023; Plata-Martinez et al., 2021; Takemura, Okuwaki, et al., 2020; Vaca et al., 2018). Interactions between megathrusts and slow earthquakes have also been reported in various regions (e.g., Baba et al., 2020; Kato et al., 2012, 2016; Vaca et al., 2018;

Voss et al., 2018). Therefore, the activity patterns and physical mechanisms of slow earthquakes have been studied. Slow earthquakes obey a scaling law that differs from that of ordinary earthquakes (Ide et al., 2007; Ide & Beroza, 2023). Thus, slow earthquakes may be controlled by physical mechanisms that are different from those of ordinary earthquakes. Slow earthquakes can be observed in the seismic and geodetic data. In this study, we focused on slow earthquakes detected by seismometers, called “seismic slow earthquakes.” Because of noise signals at microseism (0.1–1 Hz) bands, seismic slow earthquakes appear separately in the 0.01–0.1 and 1–10 Hz bands. The lower- and higher-frequency seismic slow earthquakes are referred to as very low-frequency earthquakes (VLFs) and low-frequency earthquakes (LFEs), respectively. Tremors can be considered successive occurrences of LFEs (Brown et al., 2009; Ide, 2021; Shelly et al., 2007). Swarms of LFEs/tremors and VLFs during geodetic slow earthquakes (slow slip events) have often been observed (e.g., Bartlow et al., 2011; Itoh et al., 2022; Obara et al., 2004; Rogers & Dragert, 2003). The observed characteristics of slow earthquakes in various subduction zones have been summarized in review papers (Beroza & Ide, 2011; Tomoaki Nishikawa et al., 2023; Obara, 2020; Obara & Kato, 2016; Schwartz & Rokosky, 2007).

The source parameters of seismic slow earthquakes have been extensively studied worldwide to discuss their physical characteristics. The seismic moments of seismic slow earthquakes can be obtained from an analysis of the VLFE frequency bands (Ide & Yabe, 2014; Ito et al., 2009; Maury et al., 2016, 2018; Sugioka et al., 2012; Takemura, Baba, Yabe, Emoto, et al., 2022; Takemura, Obara, et al., 2022; Takeo et al., 2010). Because seismograms in the VLFE bands have lower sensitivity to finer structural heterogeneities and can be easily simulated even for a three-dimensional (3D) model (e.g., Fichtner et al., 2009; Komatitsch et al., 2002; Maeda et al., 2017), their estimations are stable for both shallow and deep VLFEs. However, because seismic wave scattering due to small-scale (< several kilometers) heterogeneities becomes dominant at frequencies above 1 Hz (Sato et al., 2012), the source parameters of tremors cannot be deterministically estimated using the observed waveforms. Thus, the seismic energies of tremors have been estimated using smoothed velocity envelopes and the assumption of far-field body waves in an infinite homogeneous medium (e.g., Annoura et al., 2016; Maury et al., 2018; Wech, 2021; Yabe & Ide, 2014). The scaled energy, which is the ratio of the seismic energy to the seismic moment, characterizes the dynamics of earthquake faulting (Kanamori & Rivera, 2006). Owing to the observational gap of an intermediate (0.1–1 Hz) frequency band, the scaled energy of seismic slow earthquakes can be calculated as the ratio of the seismic energy of a tremor/LFE divided by the seismic moment of the accompanying VLFE.

Slow earthquakes have been detected in several regions of Japan. Deep slow earthquakes occur at depths of 30–40 km depth, near the interface of the subducted Philippine Sea Plate. These signals were observed in the inland seismic networks Hi-net and F-net (Aoi et al., 2020; National Research Institute for Earth Science and Disaster Resilience, 2019c, 2019b). The observed seismic moment rates of the deep VLFEs and the energy rates of the deep tremors are in the range of 10^{11} – 10^{12} Nm/s and 10^1 – 10^3 J/s, respectively. The scaled energy of deep slow earthquakes ranges from 10^{-10} to 10^{-9} (Ide et al., 2008; Ide & Maury, 2018; Ide & Yabe, 2014), significantly less than that of ordinary earthquakes (approximately 3×10^{-5} ; Ide & Beroza, 2001). Such a 4-order difference in the scaled energy between ordinary and slow earthquakes also suggests different governing mechanisms for both slip phenomena.

Permanent networks of ocean bottom seismometers (OBSs) have been in development since 2010 (see Aoi et al., 2020; National Research Institute for Earth Science and Disaster

Resilience, 2019a, 2019d). These networks enable us to investigate the source properties of shallow VLFs and tremors near the Nankai Trough and Japan Trench. The depths of shallow seismic slow earthquakes are ≤ 10 and 10–20 km, respectively. High-frequency seismograms at OBSs contain large site amplifications due to the low-velocity sediments beneath the OBSs. Figure 1a shows sample waveforms at the offshore DONET (M.KMD13) and inland F-net (N.KISF) stations during an intraslab earthquake. After correcting for the geometrical spreading of the body waves, the maximum amplitude at M.KMD13 was still approximately eight times larger than that at N.KISF. This was due to site amplification at M.KMD13.

Site amplification factors for an inland rock site have been estimated to accurately estimate the physical properties of offshore earthquake phenomena using OBSs. Because the signals of shallow tremors are too weak at inland rock sites (see Figure 1 of Takemura, Hamada, et al., 2023), site amplifications are typically estimated based on near-vertical incident body waves from intraslab earthquakes (blue arrows in Figure 1b). Although vertical *S*-wave amplitudes at OBSs tend to be weakly amplified, amplification factors of 5–30 against an inland rock site in horizontal components have been observed in previous studies (Kubo et al., 2018, 2020; Takemura, Emoto et al., 2023; Yabe et al., 2019). *S*-wave energy is generally dominant in horizontal components. These site amplification factors include the effects of thick sedimentary layers with V_S of 0.6–2 km/s and thin sediments of $V_S < 0.6$ km/s just below OBSs (see Figure 1b). Thick sedimentary layers beneath the DONET stations have been confirmed in seismological studies (e.g., Akuhara et al., 2020; Kamei et al., 2012; Tonegawa et al., 2017). The resolutions of sedimentary layers estimated based on seismological methods are several hundred meters. Thus, thicknesses of unmodeled thin lower-velocity ($V_S < 0.6$ km/s) sediments may be less than several hundred meters. Although the propagation paths between intraslab earthquakes and shallow tremors were expected to be significantly different (Figure 1b), the obtained site amplifications were used in site corrections for shallow tremor waveforms. After site corrections, the seismic energies of the shallow tremors were obtained in the same manner as those of the deep tremors (Nakano et al., 2019; Tamaribuchi et al., 2022; Yabe et al., 2019, 2021). The seismic energy rates of the shallow tremors range from 10^3 to 10^6 J/s. The scaled energies of shallow tremors exhibited regional differences: 10^{-9} – 10^{-8} off Cape Muroto and southeast of the Kii Peninsula and 10^{-10} – 10^{-9} off the Kii Channel and along the Japan Trench. Although these values are similar to those of deep slow earthquakes, there is a depth difference in the scaled energies (0–1 order difference) beneath and off the Kii Peninsula. This depth difference in scaled energy could be considered a result of differences in temperature and pressure at shallow (< 150 °C, < 0.2 GPa) and deep (> 300 °C, 1 GPa) depths (Yabe et al., 2019).

Recent numerical studies have revealed that the characteristics of high-frequency seismic waves around shallow plate boundaries are complicated because of thick low-velocity sedimentary layers (Takemura, Emoto, et al., 2023; Takemura, Yabe, et al., 2020). The bottom-right panel of Figure 1a shows a sample waveform of a shallow tremor. This long-duration and spindle-shaped envelope is caused not only by complicated long-duration moment rate functions but also by envelope broadening due to the thick sedimentary layer in this region. This envelope broadening can be significant if seismic sources are located just below thick sedimentary layers. Typical ordinary earthquakes tend to occur at deeper depths, and thus envelope broadening due to thick sedimentary layers becomes weak. Observations of shallow slow earthquakes are still limited in the world (summarized in Takemura, Hamada, et al., 2023), but similar phenomena can be expected in near-source OBS observations within Nankai, Mexico, Costa Rica and Hikurangi subduction zones. In these regions, shallow tremors often occur at shallower (≤ 10

km) depths (e.g., Baba et al., 2021; Plata-Martinez et al., 2021; Tamaribuchi et al., 2022; Todd et al., 2018). However, the latter effects have yet to be incorporated into conventional methods of seismic energy estimation.

In this study, to better understand seismic slow earthquakes at shallow depths, we investigated the effects of thick sedimentary layers on high-frequency seismic waves at OBSs using both observed DONET and synthetic seismograms. The Results section first provides us site amplifications at DONET stations estimated via the conventional method using observed intraslab earthquakes. These site amplifications could include both effects of thick low-velocity and thin lower-velocity sediments. We synthesized high-frequency seismograms at the OBSs from an intraslab earthquake and a shallow tremor using a wavenumber integration program code and local one-dimensional (1D) velocity models. The shallow tremors along the Nankai Trough occur around the basement of thick sedimentary layers (approximately 8km), while intraslab earthquakes tend to be located at depths of 20-40 km. We investigated the depth-dependent propagation path effects of thick sedimentary layers using synthetic seismograms with and without thick sedimentary layers. Synthetic seismograms clearly demonstrate differences in amplifications due to path effects owing to source depth. A comparison between the estimated site amplifications from observations and the effects of thick sedimentary layers from synthetics provided the major cause of the site amplifications at OBSs. We then evaluated the amplification of seismic energies for shallow tremors caused by thick sedimentary layers.

In Discussions section, we discuss seismic energy amplifications due to an invalid assumption of heterogeneities around the seismic source. The precise determination of the source depths of shallow slow earthquakes remains challenging, but the rigidity in seismic energy estimation has been typically assumed to 33 GPa as the crustal property. Seismic and scaled energies of seismic slow earthquakes were estimated in various regions of Japan. Based on the resultant seismic energy amplifications of shallow tremors, we revisited the scaled energies of seismic slow earthquakes in Japan.

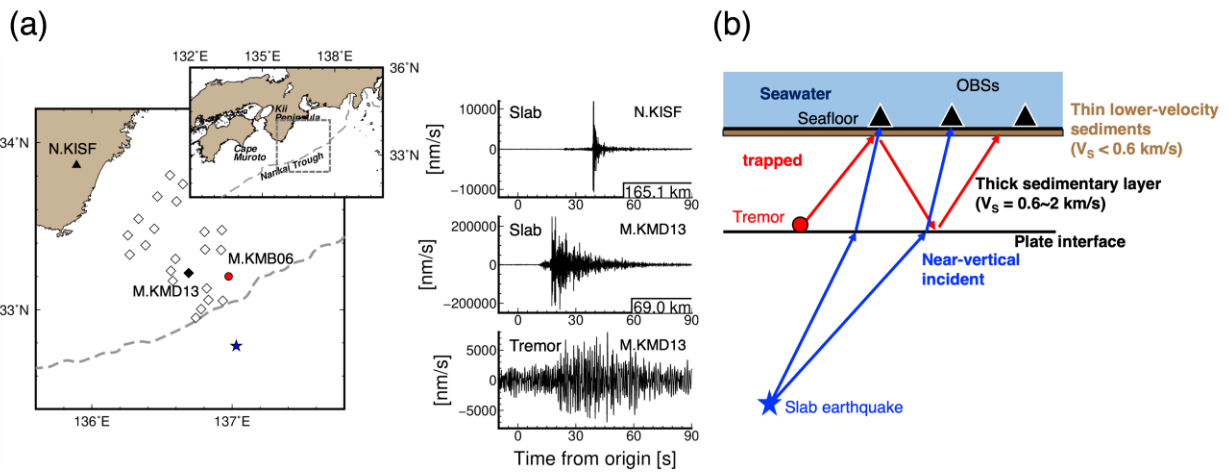


Figure 1. (a) Examples of high-frequency seismograms at offshore (M.KMD13) and inland (N.KISF) stations. The upper and middle right panels are high-frequency (> 1 Hz) EW-

component seismograms during an intraslab earthquake, which occurred at a depth of 39 km at 3:19 on May 22, 2020 (JST). The right bottom panel shows a high-frequency (> 1 Hz) EW-component seismogram during a shallow tremor, which occurred at 10:19 on December 12, 2020 (JST). The blue star and red circle represent epicenters of an intraslab earthquake and a shallow tremor, respectively. (b) Schematic illustration of propagation paths from seismic sources to OBSs southeast of the Kii Peninsula region.

2 Data and Methods

We used continuous velocity seismograms recorded at the DONET (National Research Institute for Earth Science and Disaster Resilience, 2019a) and F-net (National Research Institute for Earth Science and Disaster Resilience, 2019b) stations. Almost of F-net broadband seismometers were deployed at outcrop rock sites; thus, F-net data can be used as a reference for site correction. Takemoto et al. (2012) pointed out that the characteristics of S-wave amplifications are similar at all F-net stations for various frequency ranges. Each DONET node contains four to five seismic stations. Detailed information on both the networks is available in Aoi et al. (2020). We did not use the M.KMA and KME nodes because of their distances from the shallow tremor sources. We also did not use unburied DONET stations (KMC11 and KMC12). To estimate the site amplifications at the DONET stations, we used data from 140 intraslab earthquakes that occurred from April 2016 to December 2022. The origin time, hypocenter locations, and magnitudes were obtained from a unified hypocenter catalog provided by the Japan Meteorological Agency (JMA). The JMA magnitudes ranged 3.0–5.1. We measured the maximum *S*-wave amplitudes at the F-net and DONET stations. We estimated the site amplification factors of the DONET stations based on the method by Yabe et al. (2019). Assuming far-field body wave propagation in a homogeneous media, the *S*-wave amplitude at the *j*-th station from the *i*-th intraslab earthquake can be expressed as follows:

$$\ln(A_{ij}) = \ln(S_i) - \ln(\sqrt{4\pi}R_{ij}) - \alpha R_{ij} + \ln(G_j) \quad (1)$$

where S_i is a source term, R_{ij} is hypocentral distance, α is the attenuation factor of $\pi f/QV_s$, and G_j is a site amplification factor at the *j*-th station. We set the site amplification factor of the N.KMTF to 1. This equation can then be solved using the least-square method.

We synthesized seismograms assuming a 1D velocity structure model to investigate the propagation path effects near the Nankai Trough. The 1D *P*-wave model around the DONET stations by Nakano et al. (2013) was used. The *S*-wave velocity, density, and anelastic attenuation were obtained by assuming the empirical laws proposed by Brocher (2005, 2008). We named this model “DONET1D” (Figure 2a). In DONET1D, the interface of the Philippine Sea Plate is located at a depth of 8.07 km. DONET1D agreed with the 1D *S*-wave velocity models beneath M.KMB06 and M.KMD13 by Tonegawa et al. (2017) (blue dashed lines in Figure 2a). Thick (~ 5 km) sedimentary layers with V_s of 0.6–2.3 km/s exist beneath M.KMB and M.KMD. Using the local 3D model, Takemura, Yabe et al. (2020) and Takemura, Emoto, et al. (2023) demonstrated that the major cause of complicated high-frequency seismic wave propagation southeast off the Kii Peninsula is thick sedimentary layers, rather than other heterogeneities (such as bathymetry, the subducted Philippine Sea Plate, seawater, and small-scale velocity heterogeneities). In addition, shallow tremors and VLFE epicenters are located around the M.KMB and M.KMD nodes (Nakano et al., 2018; Takemura, Obara, et al., 2022;

Tamaribuchi et al., 2022; Yamamoto et al., 2022). Thus, modeling using DONET1D can provide the average characteristics of high-frequency seismic wave propagation within shallow tremor regions along the Nankai Trough.

To investigate the effects of thick sedimentary layers, we prepared another 1D model, DONET1D' (Figure 2b) in which the physical parameters of the sedimentary layers were replaced with those of the oceanic crust. The Green's functions using both 1D models can be evaluated by employing the wavenumber integral calculations using the open-source code "Computer programs in Seismology" (CPS; Herrmann, 2013). The seismic sources were assumed to be a low-angle thrust mechanism (strike/dip/rake = 270°/10°/90°) at a depth of 8.07 km and a normal fault mechanism (strike/dip/rake = 300°/45°/-120°) at a depth of 40 km. These are the typical mechanisms of shallow tremors and intraslab earthquakes in this region. Seismic moment M_0 was fixed at 3.98×10^{13} Nm (moment magnitude M_w 3.0).

We also simulated seismic wave propagation within the same models using the open-source finite-difference method code OpenSWPC (Maeda et al., 2017) to obtain high-frequency seismic wave propagation in 3D volumes. The 3D simulation model covered $105 \times 30 \times 75$ km³ and was discretized using a uniform grid of 0.015 km. We employed a perfectly matched layer boundary condition to reduce artificial reflections from the model boundaries. The 64-s seismic wave propagation was calculated using 80,000 time steps. In the OpenSWPC simulations, to obtain stable and accurate seismic wave propagation in 3D media, we assumed a single-cycle Küpper wavelet with a duration of 0.25 s rather than an impulse source time function (STF) to reduce numerical instability. Short-duration STFs were assumed in both CPS and OpenSWPC synthetics. The simplest tests with a short-duration test can represent seismic wave propagation from a shallow LFE source. Although short-duration seismic slow earthquakes have recently been reported (Toh et al., 2023), this assumption may be invalid for realistic tremor synthetics. Therefore, we examined the effects of complicated STFs using the Brownian slow earthquake (BSE) model (Ide, 2008; Ide & Maury, 2018).

Using theoretical S -wave traveltimes (T_S) in 1D models, we measured the maximum S -wave amplitudes for each filtered velocity seismogram from times starting at T_S-1 to reduce the effects of the zero-phase Butterworth filter. The seismic energies were calculated using smoothed velocity envelopes as a typical tremor analysis. We could not identify P and S phases from the spindle-shape tremor waveforms (Figure 1a). First, we applied a bandpass filter with passed frequencies of 2–8 Hz, which are typically used in seismic energy estimations for tremors/LFEs. The vector sum of the three-component envelopes was calculated. A 5-s moving average was applied to obtain smooth envelopes. Owing to the lack of clear P - and S -wave onsets, smoothed envelopes are typically used as S -waves for the location and energy analyses of the tremors. The half-value width, $\tau(t_2-t_1)$, of the smoothed envelope was measured as the source duration. The normalized seismic energy E_{ij}/C_{ij} at the j -th station was calculated using the following equation:

$$\frac{E_{ij}}{C_{ij}} = R_{ij}^2 \int_{t_1}^{t_2} v^2(t) dt \quad (2)$$

where R_{ij} is the hypocentral distance from the i -th source to the j -th receiver. The t_2 and t_1 are times of half-value width starting and ending, respectively. The constant, C , is expressed as follows:

$$C_{ij} = 2\pi\rho V_S \exp\left(\frac{2f_c Q^{-1} R_{ij}}{V_S}\right) \#(3)$$

where V_S is the S -wave velocity, ρ is density, f_c is the central frequency, and Q is a quality factor. In previous studies, V_S and ρ were typically fixed as 3.5 km/s and 2.7 g/cm³, respectively. These values are based on the assumption of far-field body wave propagation in an infinite homogeneous medium with a rigidity of 33 GPa. The effects of the source radiation pattern were also neglected because of high-frequency seismic wave propagation at regional distances (Takemura et al., 2009, 2016; Takemura, Yabe, et al., 2020; Trugman et al., 2021). We evaluated E_{ij}/C_{ij} for DONET1D and DONET1D' because C_{ij} became common at stations with the same distances. The estimated Q at 2–8 Hz was approximately 800 (results shown in the next section) and was not dominant in the energy estimation.

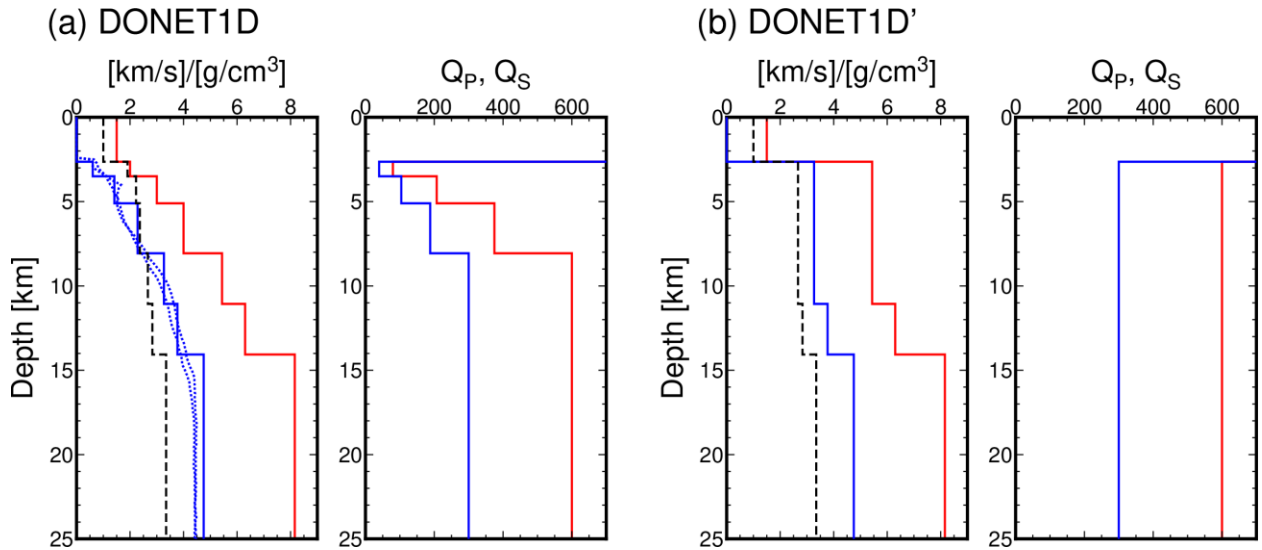


Figure 2. Assumed 1D velocity structure models. (a) DONET1D model constructed from the 1D P -wave model of Nakano et al. (2013) and empirical laws of velocity structures (Brocher, 2005, 2008). (b) DONET1D', where physical parameters within sedimentary layers are replaced with those within the oceanic crust. The red and blue colors represent P - and S -waves, respectively. The dashed lines are density as a function of depth. The blue dotted lines in (a) are S -wave velocity models beneath M.KMB06 and M.KMD13 (locations shown in the map of Figure 1a) by Tonegawa et al. (2017).

3 Results

3.1. Site amplifications at DONET OBSs based on the conventional method

Figure 3 shows the estimated site amplification factors at the F-net and DONET stations. Both vertical and horizontal site amplifications at N.KMTF (bold diamonds) were fixed as 1. We estimated the site amplifications of the 1–2, 2–4, and 4–8 Hz frequency bands. We additionally estimated those at frequencies of 2–8 Hz because the analysis of tremor signals is typically

performed using this frequency band. Our site amplification factors agree well with those in previous studies (Kubo et al., 2018; Yabe et al., 2019). The amplification factors of the horizontal component range from 5 to 40, while those of the vertical component range from 0.5 to 3, except for the stations near the Nankai Trough. Differences between the horizontal and vertical components were also reported for the *S*-wave coda H/V ratio by Takemura et al. (2023). The estimated *Q* values at 1–2, 2–4, 4–8, and 2–8 Hz were 254, 481, 933, and 795, respectively. The estimated site amplifications and *Q* values were obtained from the Zenodo repository (see “Open Research”).

3.2. Characteristics of synthetic seismograms with/without thick sedimentary layers

Figure 4 shows the synthetic velocity seismograms of DONET1D and DONET1D'. A bandpass filter with frequencies of 2–8 Hz was used. The seismic waves from a shallow tremor source were effectively trapped within thick sedimentary layers (Takemura, Yabe, et al., 2020); consequently, the onset of the *P*- and *S*-waves became unclear, and strong envelope broadening occurred (Figure 4a). In the model without sedimentary layers (Figure 4b), clear *P*- and *S*-wave onsets were observed. *sP* converted and multiple reflected waves from the sea surface were observed. From Movies S1 and S2, we can confirm the characteristics of the seismic wave propagation mentioned above. Reverberations within the sedimentary and seawater layers were clearly imaged in the simulated wavefield (Movie S1). However, we could not recognize individual phases from the results of DONET1D (Figure 4a). For a slab earthquake source (Figure 4c, d), although the traveltimes of the *P*- and *S*-waves were delayed because of the thick sedimentary layer, *P* and *S* wavetrains were clearly identified in both models. Movies S3 and S4 present the seismic wave propagation for intraslab earthquake cases.

3.3. Amplifications of maximum *S*-wave amplitudes and seismic energies

Examples of the filtered seismograms for a shallow tremor source are shown in the top panels of Figure 5. Unclear *P*- and *S*-wave onsets and envelope broadening are observed in DONET1D (blue lines). Envelope broadening in the smoothed envelopes of DONET1D (blue bold lines in Figure 5) is caused by the contamination of reflected *S*-waves between the seafloor and basement of the sedimentary layers (plate interface). These reflected *S*-waves contaminate the smoothed tremor envelopes of DONET1D. In DONET1D' (red lines), *P*- and *S*-wave signals were clear and impulsive. The reflection phases from the sea surface were repeatedly confirmed after *S* arrival. The smoothed envelopes in DONET1D' (red bold lines) contain not only the *S*-wave content but also those of *P*- and reflected waves from the sea surface. At an epicentral distance of 20 km, the maximum amplitude of the smoothed envelope in DONET1D was several times larger than that of DONET1D'. This amplitude difference decreased at a distance of 40 km; however, the envelope duration in DONET1D remained longer.

Figure 6 shows the maximum *S*-wave amplitudes at 1–2, 2–4, and 4–8 Hz for the shallow tremor and intraslab earthquake. The blue and red symbols represent the results from DONET1D and DONET1D', respectively. For an intraslab earthquake, the differences in the horizontal maximum *S*-wave amplitudes between DONET1D and DONET1D' were practically constant irrespective of the distance. The differences in an intraslab source between DONET1D and DONET1D' decreased with increasing frequency. The ratios of the horizontal maximum *S*-wave

amplitudes between DONET1D and DONET1D' were approximately 1–2 at 1–2 and 2–4 Hz, implying that the observed large horizontal amplifications (Figure 3) were mostly caused by thin lower-velocity ($V_S < 0.6$ km/s) sediments just below the DONET stations (brown areas in Figure 1b). These distance-independent differences can easily be corrected using the estimated site amplification factors from a method assuming far-field *S*-wave propagation. However, complicated differences in the maximum *S*-wave amplitudes between the models appeared for a shallow tremor source (Figure 6b). At 1–2 and 2–4 Hz, the horizontal *S*-wave amplitudes were 2–13 times amplified at distances of 5–20 km (near-source OBSs). The differences in horizontal *S*-wave amplitudes also decreased with increasing frequency and distance. The effects of thick sedimentary layers on the maximum *S*-wave amplitudes for shallow tremors and intraslab earthquakes differed completely.

Figure 7 shows the normalized seismic energy E/C at each distance. As previously mentioned, the seismic energies of shallow tremors were evaluated using velocity envelopes at 2–8 Hz. Although an impulse STF was assumed in the CPS synthetics, a 10-s half-value width (dashed lines in the right panels in Figure 7) was expected because of the 5-s moving average smoothing. As C is common at stations at the same distance, the ratios of the seismic energies of DONET1D and DONET1D' (amplification factor for seismic energy) (Figure 8) reflect the amplification factors of the seismic energies at each station. The differences for an intraslab earthquake (Figures 7a and 8a) were nearly constant (2–3 times), irrespective of the distance. These results indicate that the seismic energies for an intraslab earthquake can be estimated using the conventional method. Distance-dependent features of seismic energy amplification were observed for the shallow tremor source (Figures 7b and 8b). At distances of ≤ 5 km (the region just above a source), we observed an amplification factor of approximately 4. This is slightly larger than that of an intraslab source (3.3) but can be considered a vertical incident amplification factor. Large (> 5) seismic energy amplifications were observed at distances of 5–20 km. Reflected *S*-waves from the sediment/oceanic crust boundary (plate boundary) appeared repeatedly (Movie S1) in DONET1D, although such phases were not observed in DONET1D' (Movie S2). The smoothed velocity envelopes in DONET1D contained such reflections; consequently, large energy amplifications occurred at distances of 5–20 km.

According to previous studies of shallow slow earthquakes (Masaru Nakano et al., 2018; Sugioka et al., 2012; Takemura et al., 2019; Takemura, Hamada, et al., 2023), we considered that shallow tremors could be molded by a low-angle thrust faulting mechanism around the plate boundary. In this case, *S*-wave energies can be weakened at distances of 5–20 km due to the four-lobe *S*-wave source radiation pattern (red symbols in Figures 6b and 7b). Four-lobe *S*-wave amplitude pattern are gradually distorted as increasing frequency and distance because of seismic wave scattering due to small-scale heterogeneities (e.g., Imperatori & Mai, 2013; Morioka et al., 2017; S. Takemura et al., 2009, 2016). Takemura, Yabe, et al. (2020) demonstrated that in the cases of seismic sources just below or within thick sedimentary layer, trapping seismic wave energies within thick sedimentary layers also cause distortion of four-lobe *S*-wave amplitude pattern. Thus, significant amplifications of seismic energies for shallow tremor appear at distances of 5–20 km. At distances > 20 km, *S*-waves propagated horizontally, and the amplification of seismic energy weakened with increasing distance. Seismic energy amplifications of a shallow tremor at distances less than 5 km are similar as those for an intraslab earthquake.

Stronger attenuation compared with the empirical law has been estimated at shallower depths (e.g., Abercrombie, 1997; Eberhart-Phillips et al., 2014; Yoshida et al., 2023). Thus, we additionally synthesized seismograms using DONET1Dq, where Q_s value within the shallowest layer was replaced from 39.8 to 20. Figure S1 shows seismic energy amplifications of DONET1Dq. Amplifications of seismic energies become weaker from the original DONET1D, but amplifications due to the propagation path within thick sedimentary layers are still significant at epicentral distances of 5–20 km. Although our knowledge of Q_s structures at shallower depths is limited, propagation-path amplification tends to be dominant in shallow tremor seismograms at distances of 5–20 km.

To evaluate the effects of the STFs, we synthesized them based on the BSE model (Ide, 2008; Ide & Maury, 2018). We prepared 200 BSE model STFs with a characteristic time α of 0.01 s^{-1} , which were normalized as each seismic moment of 1. These STFs were convolved using Green's functions in DONET1D and DONET1D'. The resultant ratios of the seismic energies of DONET1D and DONET1D' are illustrated in Figure 9a. Figure 9b shows two examples of BSE model STFs. The duration of the prepared BSE model STFs ranged from 1–54 s (Figure 9c). Although fluctuations in seismic energy ratios were recognized (Figure 9a), large amplifications of seismic energies at distances of 5–20 km were commonly observed. The strength of the envelope broadening appears to depend on the source duration (solid, dashed, and dotted lines in Figure 9d). Parameters τ and τ_0 are the half-value widths of the synthetic envelopes from DONET1D and DONET1D', respectively. The BSE model STFs with shorter durations exhibited strong envelope broadening (large $(\tau - \tau_0)/\tau_0$), as shown by the results of an impulse STF (bold blue line in Figure 9d). With increasing source duration, the effects of envelope broadening caused by the thick sedimentary layer tended to be relatively weak (blue dashed and dotted lines). For the longest duration STF case (blue dotted line), nearly similar half-value widths ($(\tau - \tau_0)/\tau_0 \approx 0$) were measured in both models. If source durations are sufficiently longer than the envelope widths of Green's functions, the strength of envelope broadening caused by thick sedimentary layers becomes relatively weak; consequently, overestimations of source durations are negligible.

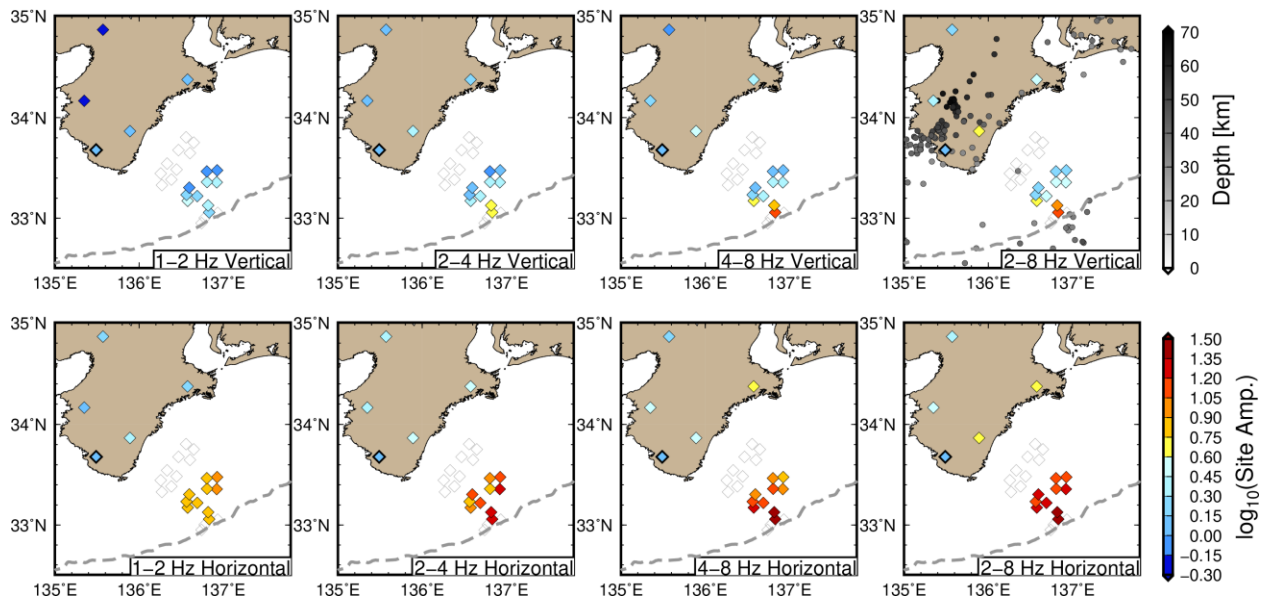


Figure 3. Spatial variations of site amplification factors at each frequency band. The upper and bottom panels are site amplification factors for vertical and horizontal components, respectively. The gray circles in the upper right panel are epicenters of slab earthquakes used in estimating site amplification factors. The diamond enclosed by the bold line is the reference site N.KMTF (the site amplification factor of N.KMTF was fixed as 1).

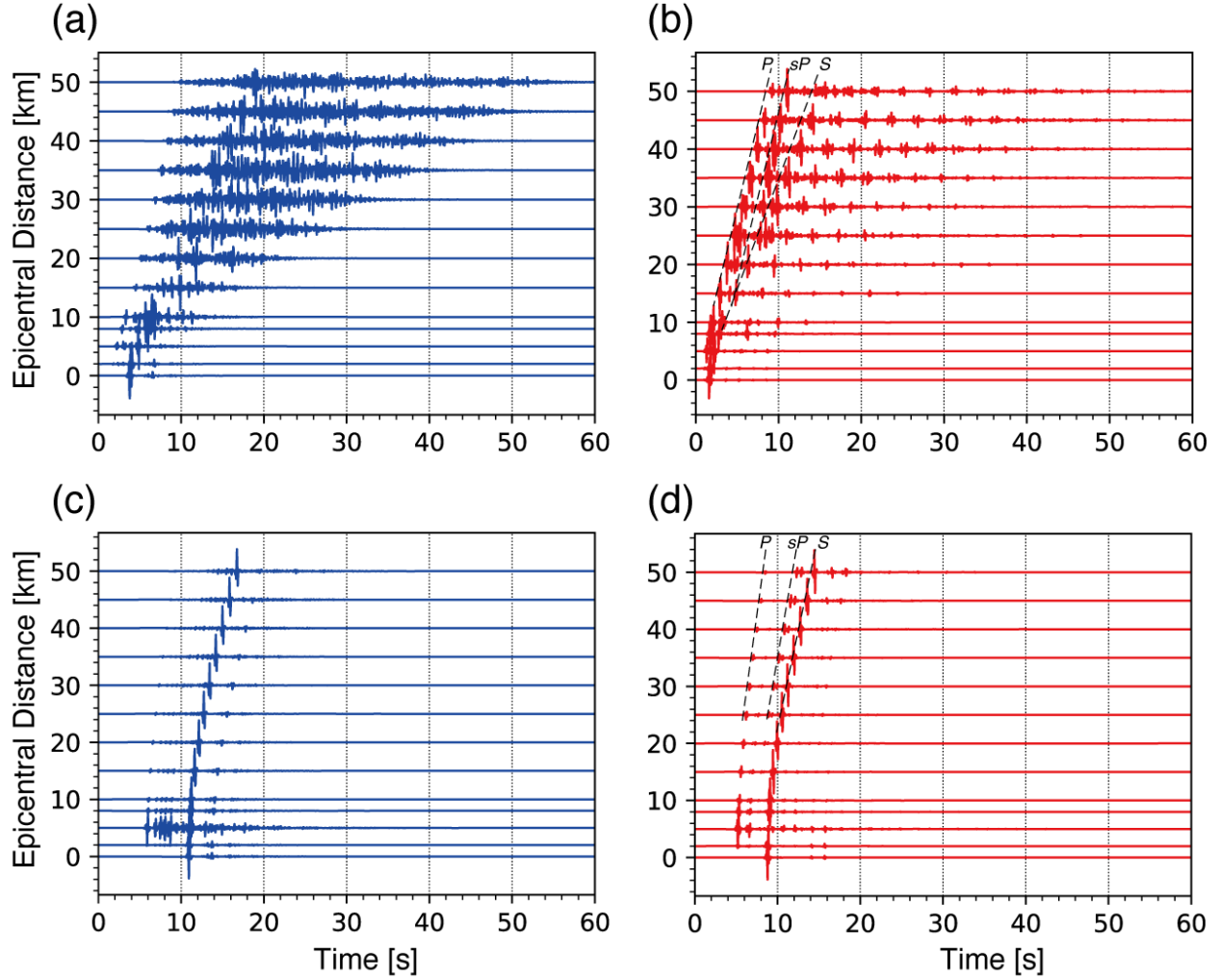


Figure 4. Radial component velocity seismograms synthesized using CPS. The seismic sources in (a, b) and (c, d) are a shallow tremor and intraslab earthquake, respectively. The source time functions of each case are an impulse. (a, c) DONET1D and (b, d) DONET1D'. We applied a bandpass filter of 2–8 Hz, and maximum amplitudes at each trace were normalized.

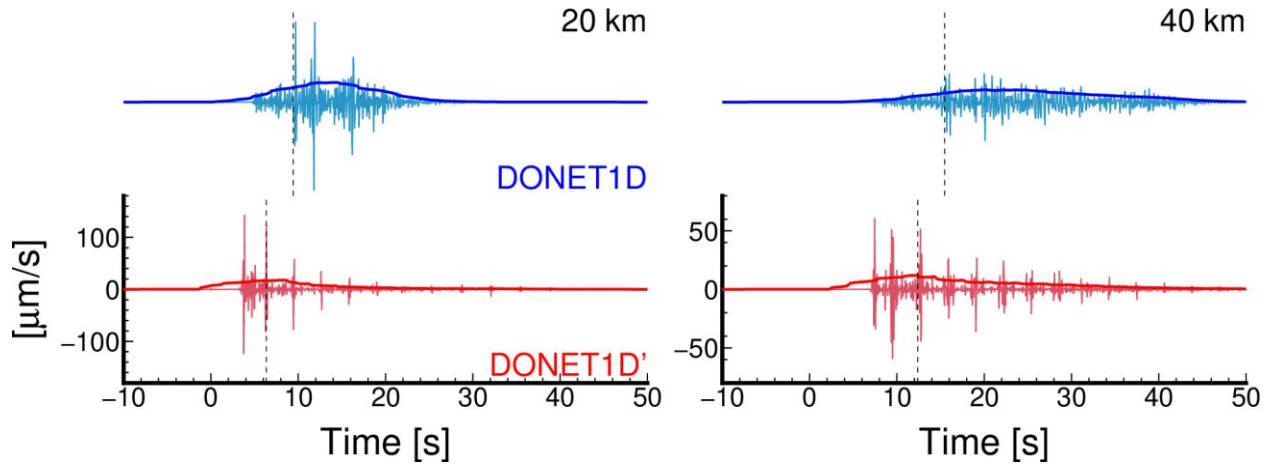


Figure 5. Examples of Green's functions at distances of 20 and 40 km for a shallow tremor source. The radial component velocity traces were filtered with a passed frequency of 2–8 Hz. The bold lines are smoothed velocity envelope traces. The black dashed lines represent theoretical *S*-wave travel times in each model.

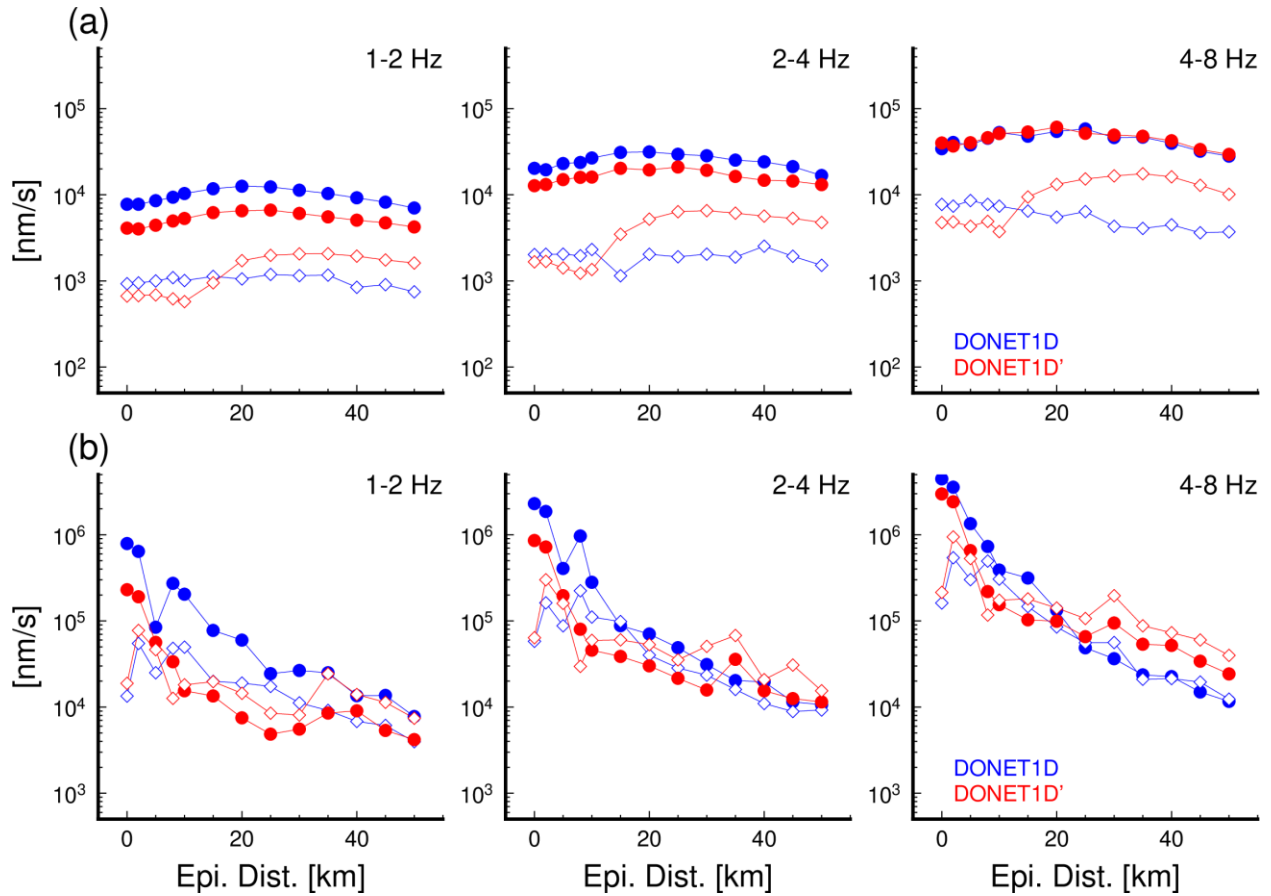


Figure 6. Maximum *S*-wave amplitudes at each frequency band from (a) intraslab earthquake and (b) shallow tremor sources. The blue and red symbols are the maximum *S*-wave amplitudes

in DONET1D and DONET1D', respectively. The filled and open symbols are those in horizontal and vertical components, respectively.

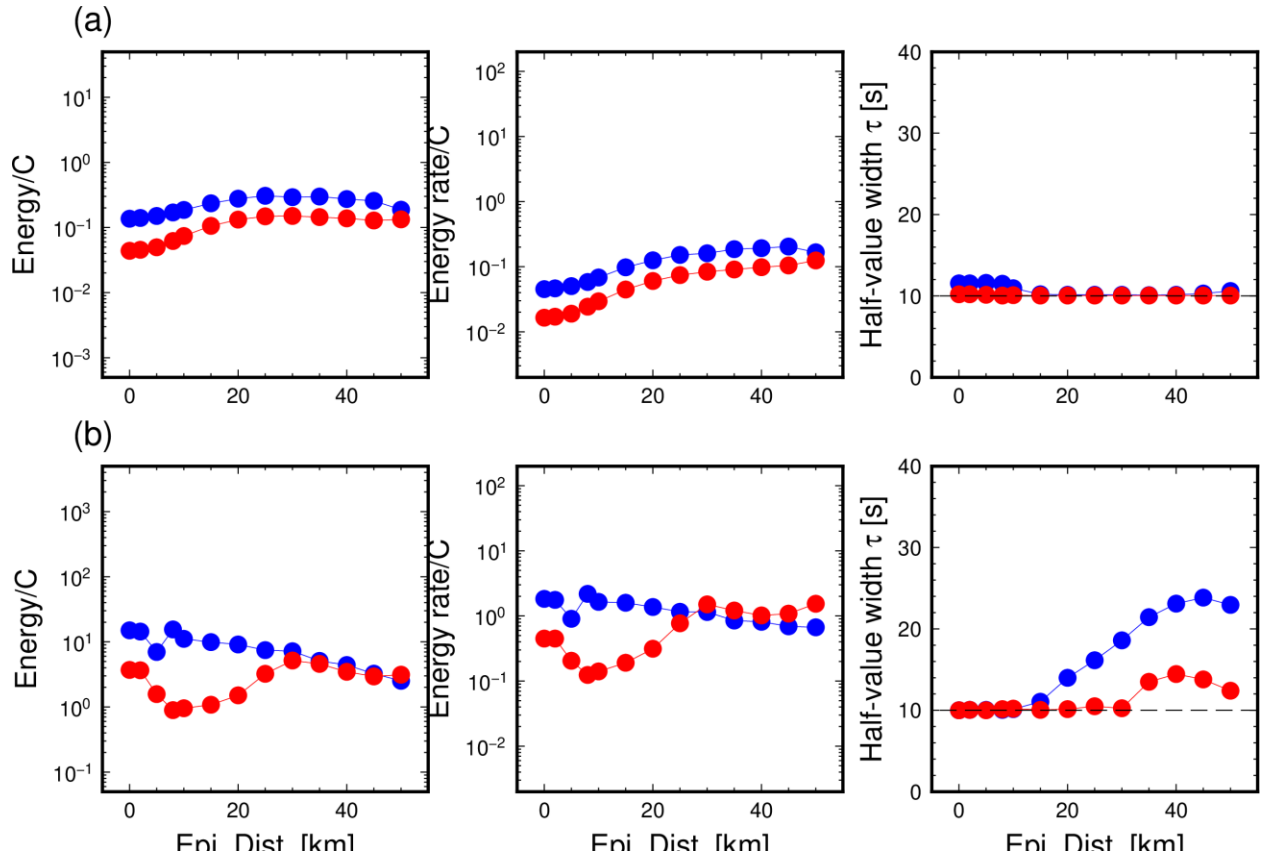


Figure 7. Normalized seismic energies of (a) intraslab earthquake and (b) shallow tremors. Normalization factor C includes physical parameters and anelastic attenuation. The blue and red symbols represent the results of DONET1D and DONET1D', respectively.

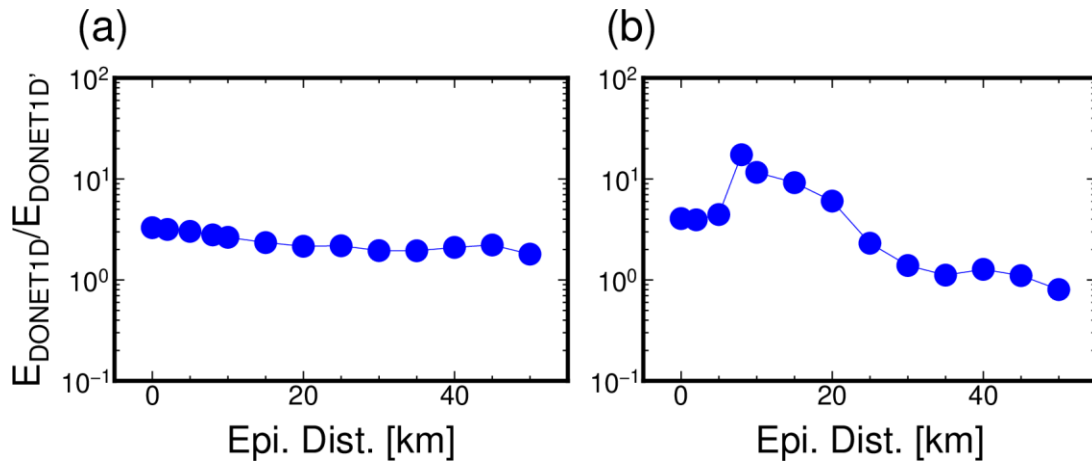


Figure 8. Ratio of seismic energies between DONET1D and DONET1D' for (a) intraslab earthquake and (b) shallow tremor sources.

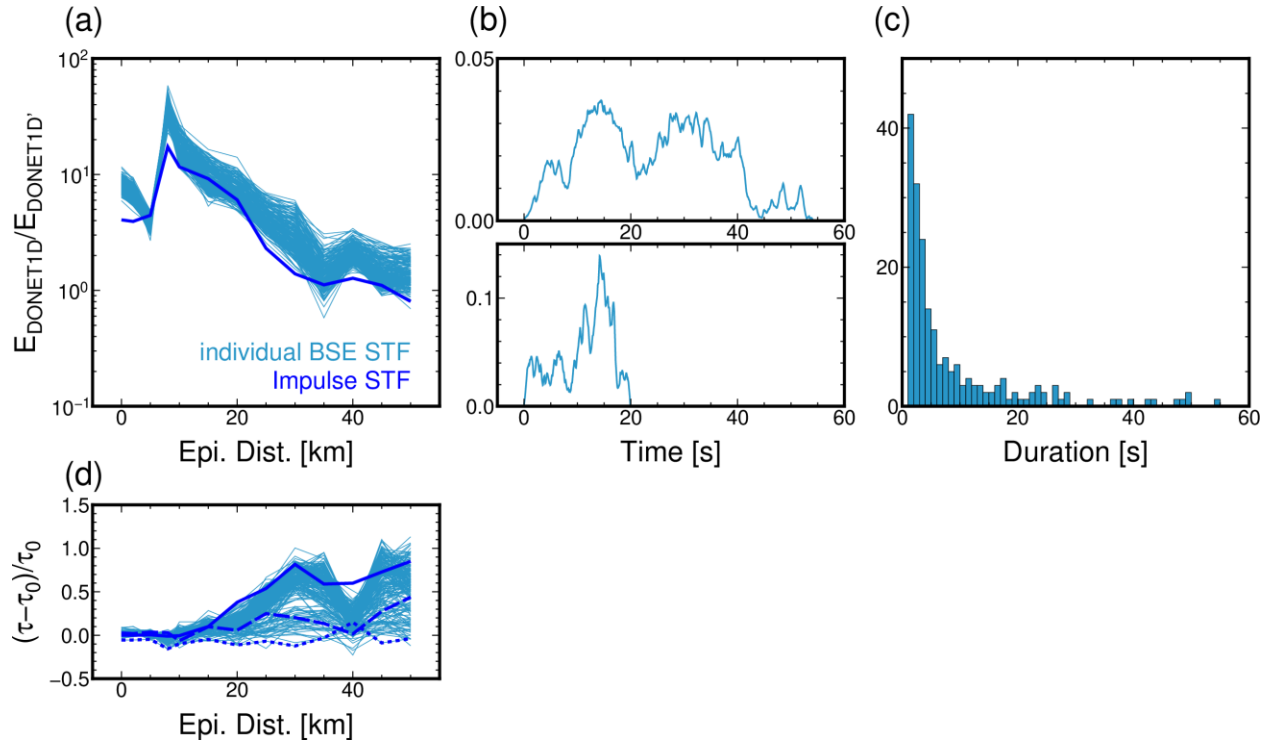


Figure 9. Ratio of seismic energies of shallow tremor using the Brownian slow earthquake (BSE) model with a characteristic time of $\alpha = 0.01 \text{ s}^{-1}$. (a) The ratio of seismic energies between DONET1D and DONET1D' for the BSE model and impulse STF (Green's function), (b) examples of BSE model STF, and (c) durations of used BSE model STFs. The light blue lines in (a) represent ratios of seismic energies between DONET1D and DONET1D' for individual BSE model STFs. The blue bold line is the same as in Figure 8b. (d) Estimated half-value width ratio between DONET1D (τ) and DONET1D' (τ_0). The blue bold, dashed, and dotted lines in (d) are ratios of impulse STF, BSE model STF with a duration of 17 s, and the longest BSE model STF (54 s), respectively.

4 Discussion

The characteristics of seismic energy amplification caused by thick sedimentary layers differ between intraslab earthquakes and shallow tremors. Large amplifications at distances of 5–20 km cannot be corrected using site amplification factors based on conventional methods. Owing to the signal-to-noise ratio of shallow tremors at OBSs, near-source (≤ 20 km) OBSs are selected for analysis. Based on seismic energy amplifications due to thick sedimentary layers (Figure 8b), we should correct additional 0.5–1 order amplifications in seismic energies of shallow tremors in previous studies along the Nankai Trough. This amplification correction is valid when shallow tremors occur at the plate interface.

4.1. Effects of invalid rigidity assumption on seismic energy estimation

Slow earthquake phenomena are considered slip phenomena at the plate boundary. Although the precise determination of the source depths of shallow slow earthquakes remains challenging, shallow VLFs tend to be located within underthrust sediments around the décollement (Akuhara et al., 2020; Sugioka et al., 2012; Yamamoto et al., 2022). Underthrust sediments are considered to have low seismic velocity (1–2 km/s). In this situation, is the assumption of 33 GPa rigidity ($V_S = 3.5$ km/s and $\rho = 2.7$ g/cm³) in the conventional seismic energy estimation valid? We investigated the structural dependency of the source region in the seismic energy estimation. We synthesized Green's functions at depths of 6.0 and 9.0 km. The former and latter sources are located within the underthrust sediment ($V_S = 2.3$ km/s) and oceanic crust layer 2 ($V_S = 3.3$ km/s). We fixed a focal mechanism and a seismic moment of 3.98×10^{13} Nm, as in previous synthetics.

In all synthetics, relatively large amplifications were observed at distances of 5–20 km. Based on these results, we concluded that amplifications caused by path effects of the thick sedimentary layers were dominant at distances of 5–20 km because the reflected *S*-waves from the plate interface had sufficient amplitudes. In such cases, the energies of the reflected *S*-waves are contaminated within a half-value width time window of smooth envelopes; consequently, the seismic energies of shallow tremors tend to be overestimated.

Although the effects of multiple *S*-wave reflections commonly appear at distances of 5–20 km, the level of seismic energy amplification increases with decreasing source depth. This is because of the differences in rigidity between DONET1D and DONET1D'. Although the seismic moment was fixed as 3.98×10^{13} Nm, and the rigidity of DONET1D' was constant (28 GPa) at depths shallower than 11 km, the rigidities of the source regions at depths of 6 and 9 km in DONET1D were 12 and 28 GPa, respectively. Although a double-couple source could not be strictly assumed at the plate boundary, the rigidity at a depth of 8.07 km (plate interface) was 28 GPa, just below the underthrust sediments (12 GPa). Thus, the intermediate features between the 6- and 9-km sources. These rigidity differences could be another cause of seismic energy amplification, assuming far-field *S*-wave propagation in an infinite medium with a rigidity of 33 GPa. The precise spatial distribution of rigidity is also important for seismic moment estimation (Figures 4, 5, and 7 in Takemura et al., 2021). Although the seismic moment is proportional to the observed amplitudes, the seismic energy is calculated by temporal integration of the square velocity amplitudes. Thus, the effects of incorrect rigidity assumptions are more severe in the seismic energy estimation.

4.2. Propagation path amplifications along the Japan Trench

The seismic and scaled energies of slow earthquakes were also evaluated along the Japan Trench, offshore regions of northeastern Japan, and Hokkaido (Yabe et al., 2021). These were calculated using the OBS network (S-net), assuming far-field body wave propagation in an infinite medium. We also synthesized velocity seismograms using a 1D velocity model around the Japan Trench to validate their estimations. The 1D model was constructed from a 1D depth profile at 143.6 °E and 40.0 °N from the local 3D model of Koketsu et al. (2012). The region at 143.6 °E and 40.0 °N is approximately the centroid of tremor activity. We refer to this model as NEJP1D. We also constructed NEJP1D' in which the physical parameters of the sedimentary layers in NEJP1D were replaced with those of the crust. The source of the tremor was located at a depth of 12.85 km. The ratios between NEJP1D and NEJP1D' (Figure 11a) were stable (3.5–7) compared with those along the Nankai Trough (Figure 8b). We also plotted energy amplifications for an intraslab earthquake (diamonds in the middle panel of Figure 11a). Because of differences in focal mechanisms and incident angles to the basement, amplifications for an intraslab earthquake were more stable and larger, but distant-independent features commonly appeared in both cases. The differences of seismic energy amplifications between tremors and intraslab earthquakes were weaker compared with those along the Nankai Trough (Figure 8). Thus, the conventional method, which assumes far-field body wave propagation, practically works in the Tohoku region. This is because the tremors occurred sufficiently deeper than the basement of the sedimentary layer (Figure 11b). The differences in the propagation paths between tremors along the Nankai Trough and Japan Trench are illustrated in Figures 1b and 11b.

The signal-to-noise ratio of shallow tremors is typically low at OBSs far from their sources. Thus, near-source (≤ 20 km) OBS data are often selected in seismic energy estimations of shallow tremors. In addition, site amplifications from the conventional method (Figure 3) are mostly controlled by thin lower-velocity (< 0.6 km/s) sediments just below stations. Based on the above synthetic studies and the selected use of near-source OBSs, we conclude that approximately 0.5–1.3 order overestimations can occur in the seismic energy estimation of shallow tremors along the Nankai Trough (Figures 8 and 10). These overestimations were caused by propagation path effects and an invalid rigidity assumption. Similar overestimations are expected for shallow slow earthquakes in the regions of Hikurangi, Mexico, and Costa Rica if near-source OBSs are used. Shallow slow earthquakes are located near the trough or shallower (≤ 10 km) depths (Baba et al., 2021; Plata-Martinez et al., 2021; Todd et al., 2018; Walter et al., 2013). Although slow earthquakes are generally phenomena of faulting on the plate boundary, amplifications are typically more severe if shallow tremors occur within sedimentary layers.

4.3. Scaled energy of seismic slow earthquakes at deep and shallow depths around Japan

Based on the above results, we revisited the scaled energy of slow earthquakes. Figure 12 shows the relationships between the seismic energy and moment rates for slow earthquakes in various regions. Deep slow earthquakes in the Nankai, Mexico, and Cascadia subduction zones were obtained from previous studies (Ide, 2016; Ide & Maury, 2018; Ide & Yabe, 2014). We also plotted the relationship between the moment and seismic energy rates of slow earthquakes along the Japan Trench (Yabe et al., 2021). Based on the effects of the thick sedimentary layer around the shallow slow earthquake sources along the Nankai Trough, we performed a 1 order

correction for the seismic energy rates of shallow tremor and a 0.3 order correction for the seismic moment rate of shallow VLFs along the Nankai Trough from the results in Yabe et al. (2019, 2021). The 0.3 order corrections of the seismic moment rates of the shallow VLFs were determined by the rigidity difference between the oceanic crust (28 GPa) and underthrust sediments (12 GPa). The rigidity of the oceanic crust is almost twice that of underthrust sediments, and a two-fold amplification of the VLFE signals is expected. Temperature and lithostatic pressure at deep depths are 150–500 °C and 0.7–1.7 GPa, which are significantly larger than those at shallower depths (< 150°C and < 0.2 GPa) (Behr & Bürgmann, 2021; Saffer & Wallace, 2015; Syracuse et al., 2010). Even for these large differences in tectonic environments, we concluded that the scaled energies of seismic slow earthquakes range from 10^{10} to 10^{-9} , irrespective of region and depth (filled symbols in Figure 12).

An $Mo \propto T$ scaling law was suggested in 2007 (Ide et al., 2007) using limited catalogs. Recently, Ide & Beroza (2023) revisited the scaling law of slow earthquakes using the updated catalogs of slow earthquakes worldwide. They suggested an $Mo \propto T$ upper-bound scaling law for deep slow earthquakes in various subduction zones. However, the relationships of detectable shallow VLFs between seismic moments and durations along Nankai Trough (Sugioka et al., 2012; Takemura et al., 2019; Takemura, Obara, et al., 2022) are slightly different with an $Mo \propto T$ upper-bound scaling law for deep slow earthquakes. Shallow VLFs lie between scaling laws of ordinary ($Mo \propto T^3$) and deep slow ($Mo \propto T$) earthquakes. The detectability of VLFs along the Nankai Trough was evaluated in Takemura, Baba, Yabe, Yamashita, et al. (2022). Duration ranges were not different at different depths, but the seismic moments of shallow VLFs were 1–2 orders larger than those at deeper depths (Ide et al., 2008). A similar trend has been reported in Costa Rica (Baba et al., 2021). Other differences between shallow and deep slow earthquakes (durations and recurrent intervals of slow earthquake episodes, migration speeds, etc.) were summarized in a recent review paper (Takemura, Hamada, et al., 2023). Despite the different scaling laws between deep and shallow slow earthquakes, our study suggests that the scaled energies of seismic slow earthquakes are common (10^{-10} – 10^{-9}), irrespective of depth and region. What factors cause the different distributions of seismic moments and durations at shallow and deep depths? Source analysis of seismic slow earthquakes under valid assumptions should be addressed in future studies to answer this question. The integration of seismological, geodetic, geological, and experimental studies is indispensable for investigating the source physics and tectonic environments of slow earthquakes.

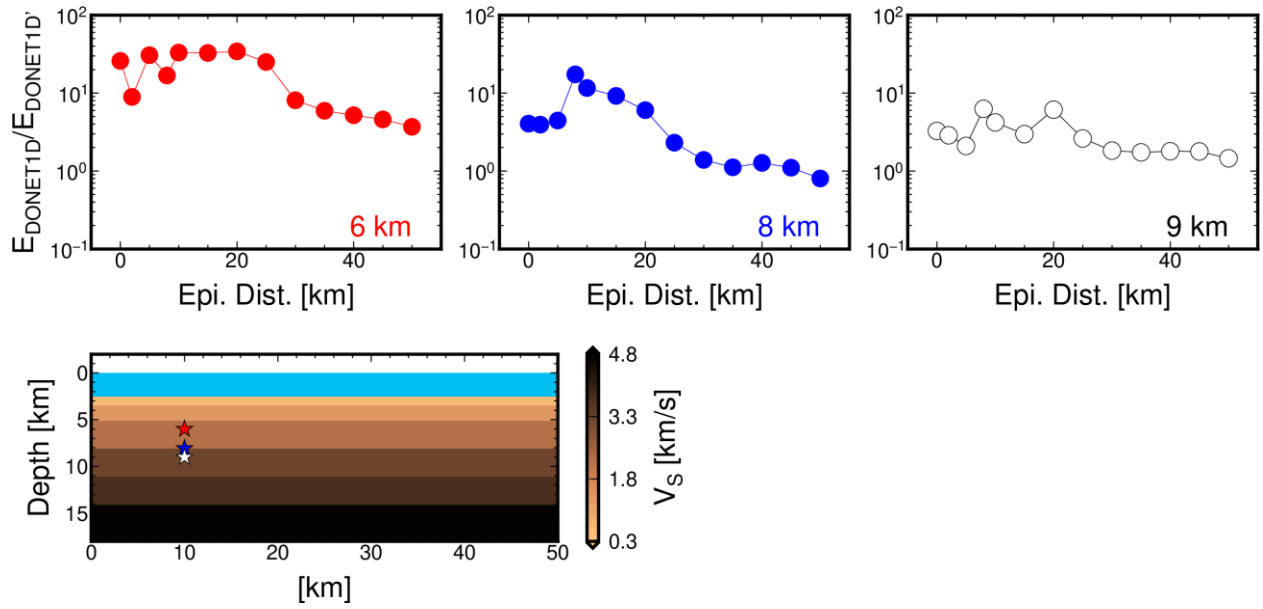


Figure 10. Seismic energies of shallow tremors at depths of 6 (within the sedimentary layer), 8.07 (plate boundary), and 9 km (within the 2nd layer of the oceanic crust).

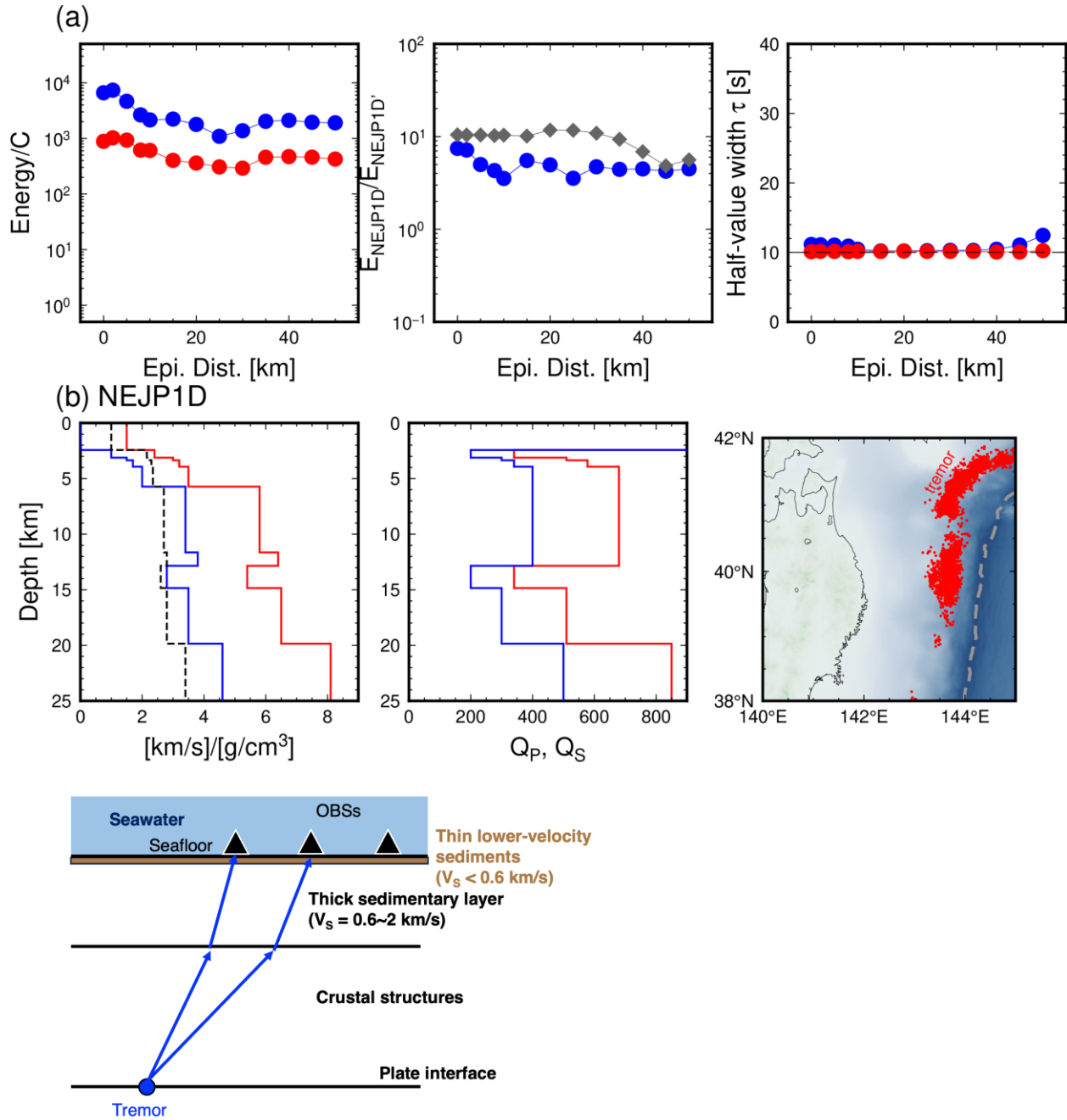


Figure 11. Seismic energies of synthetic tremor envelopes along the Japan Trench. (a) Seismic energies (E/C), ratio of seismic energies, and half-value width (duration) of NEJP1D and NEJP1D'. In the middle panel of (a), ratio of seismic energies of an intraslab earthquake (40 km depth) between NEJP1D and NEJP1D' are also plotted by diamonds. (b) NEJP1D model. The red and blue colors represent P - and S -waves, respectively. The dashed lines represent density as a function of depth. The right panel in (b) is the map around the Japan Trench. Tremor epicenters are referred from Nishikawa et al. (2019). The bottom panel in (b) is a schematic figure of seismic wave propagation from the tremor off Tohoku.

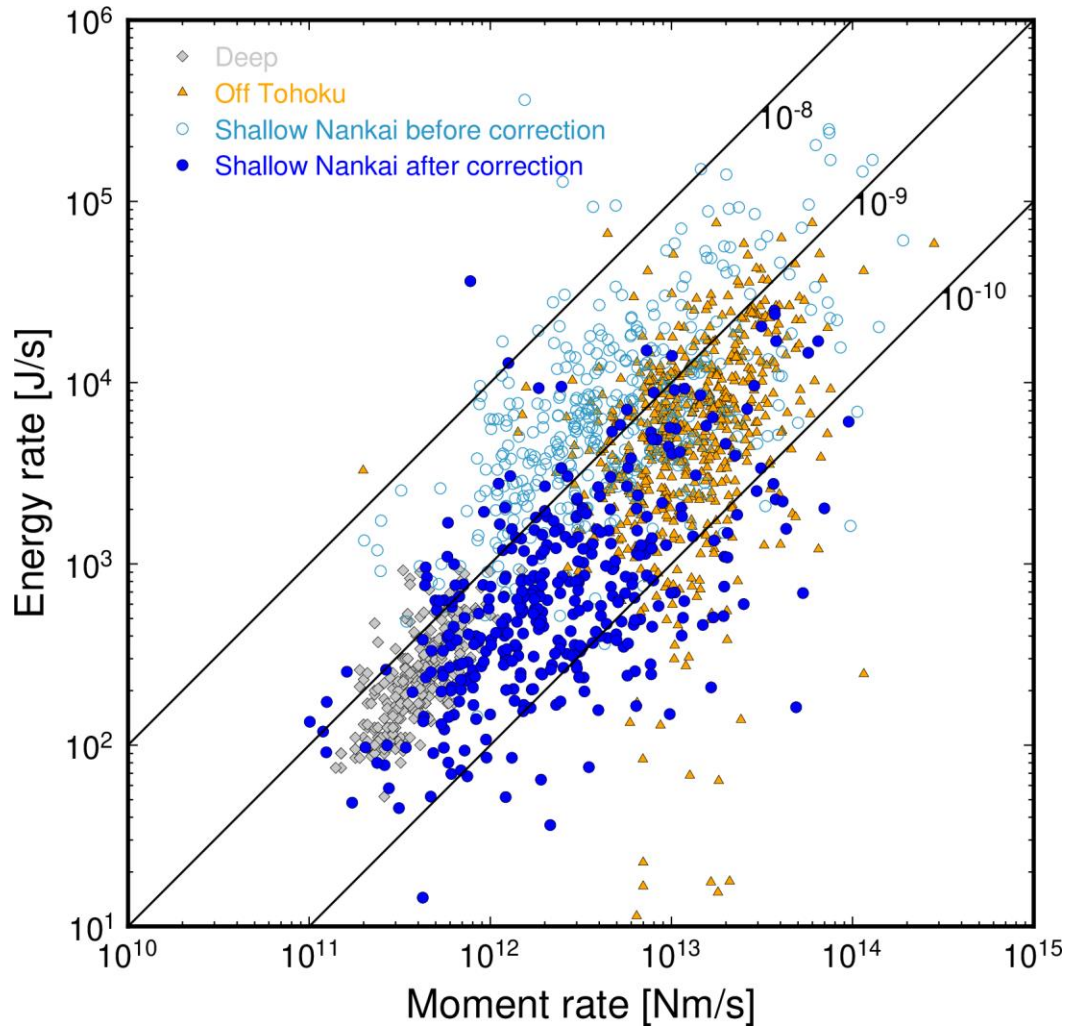


Figure 12. Revisited relationships between the seismic energy rates of tremors and seismic moments of accompanying VLFs. The gray diamonds indicate deep seismic slow earthquakes in Mexico, Cascadia, and Nankai subduction zones (Ide, 2016; Ide & Maury, 2018; Ide & Yabe, 2014). The orange triangles indicate the seismic moment and energy rates of seismic slow earthquakes off Tohoku from Yabe et al. (2021). The light blue open circles indicate the original results of shallow slow earthquakes along the Nankai Trough (Yabe et al., 2019, 2021). The blue-filled circles indicate corrected relationships between seismic moment and energy rates for shallow slow earthquakes along the Nankai Trough.

5 Conclusions

Recent studies on high-frequency seismic wave propagation have revealed that the effective trapping of seismic waves within thick sedimentary layers affects the waveforms observed at OBSs, even for near-source distances. Large envelope broadening and amplification are expected in high-frequency seismograms of OBSs. Thus, in this study, we investigated the effects of the propagation path and site amplification on seismic energy estimations for shallow tremors along the Nankai Trough.

Assuming near-vertical incidents to OBSs and far-field *S*-wave propagation, we estimated frequency-dependent site amplifications at DONET stations; the amplification factors of DONET stations in the horizontal component ranged from 5 to 40. The synthetics for an intraslab earthquake assuming a local 1D velocity model with $V_S \geq 0.6$ km/s are only 1–2 times the amplifications from a 1D model without sedimentary layers. This indicates that large amplifications at the DONET stations were primarily controlled by thin lower-velocity (< 0.6 km/s) sediments just below the DONET stations. For a shallow tremor source, 5–10 times the amplifications of seismic energy due to thick sedimentary layers appeared at near-source (≤ 20 km) distances irrespective of STF complexities. This amplification was caused by multiple reflected *S*-waves from the plate interface. Because the *S*-phase cannot be identified from typical tremor waveforms, smoothed velocity envelopes have been widely used in seismic energy analysis. In this case, multiple reflected *S*-waves were contaminated. If shallow tremors occur within underthrust sediments, the assumption of far-field *S*-wave propagation in an infinite medium with a rigidity of 33 GPa is invalid. The incorporation of precise rigidity around the source region is required.

Overestimations owing to thick sedimentary layers often occurred in the seismic energy estimations of shallow tremors near the trench. Similar overestimations using near-source (≤ 20 km) OBSs potentially occur in regions of Hikurangi, Costa Rica, and Mexico. Based on propagation path amplification at near-source OBSs and the invalid rigidity assumption, approximately 0.5–1.3 order overestimations can occur in the seismic energy estimation of shallow tremors along the Nankai Trough based on the conventional method. After correcting for overestimations of shallow tremor energy and VLFE moment rates in previous studies, the scaled energies of shallow seismic slow earthquakes along the Nankai Trough and Japan Trench and deep seismic slow earthquakes in various regions range from 10^{-10} to 10^{-9} . This means that the physical mechanisms governing seismic slow earthquakes can be the same, irrespective of region and source depth.

Acknowledgments

This study was supported by a JSPS KAKENHI Grant-in-Aid for Scientific Research (C), grant number JP21K03696, and a Grant-in-Aid for Scientific Research on Transformative Research Areas “Science of Slow-to-Fast earthquakes,” grant numbers JP21H05203 and JP21H05205. We conducted numerical simulations of seismic wave propagation in 3D models using the Earth Simulator on the *Japan Agency for Marine-Earth Science and Technology* and Wisteria/BDEC-01 on the *Information Technology Center, the University of Tokyo*. The calculation resources of Wisteria/BDEC-01 were supported by *Earthquake Research Institute, the University of Tokyo*,

Joint Research Program 2023-S-A101. The authors also acknowledge two anonymous reviewers, the associate editor and the editor Prof. R. Abercrombie, which helped to improve our manuscript.

Open Research

We used DONET (National Research Institute for Earth Science and Disaster Resilience, 2019a) and F-net (National Research Institute for Earth Science and Disaster Resilience, 2019b) data. The Python package, HinetPy (Tian, 2020), was used to download the data. CPS (Herrmann, 2013) and OpenSWPC (Maeda et al., 2017) were used for waveform synthesis. Seismic analysis codes (Goldstein & Snoke, 2005), obspy (Beyreuther et al., 2010), scipy (Virtanen et al., 2020), numpy (Harris et al., 2020), and Generic Mapping Tools (Wessel et al., 2013) were used for waveform analysis and image creation. The catalog of ordinary earthquakes used to estimate site amplification was obtained from the JMA (<https://www.data.jma.go.jp/eqev/data/bulletin/index.html>). The catalogs of slow earthquakes along the Nankai Trough were referred from the “Slow earthquake database” (Kano et al., 2018). Estimated site amplification factors at DONET stations and Movies S1-S4 are available at a Zenodo repository (Takemura, 2023).

References

- Abercrombie, R. E. (1997). Near-surface attenuation and site effects from comparison of surface and deep borehole recordings. *Bulletin of the Seismological Society of America*, 87(3), 731–744. <https://doi.org/10.1785/BSSA0870030731>
- Akuhara, T., Tsuji, T., & Tonegawa, T. (2020). Overpressured Underthrust Sediment in the Nankai Trough Forearc Inferred From Transdimensional Inversion of High-Frequency Teleseismic Waveforms. *Geophysical Research Letters*, 47(15), 0–3. <https://doi.org/10.1029/2020GL088280>
- Annoura, S., Obara, K., & Maeda, T. (2016). Total energy of deep low-frequency tremor in the Nankai subduction zone, southwest Japan. *Geophysical Research Letters*, 43(6), 2562–2567. <https://doi.org/10.1002/2016GL067780>
- Aoi, S., Asano, Y., Kunugi, T., Kimura, T., Uehira, K., Takahashi, N., et al. (2020). MOWLAS: NIED observation network for earthquake, tsunami and volcano. *Earth, Planets and Space*, 72(1). <https://doi.org/10.1186/s40623-020-01250-x>
- Baba, S., Takeo, A., Obara, K., Matsuzawa, T., & Maeda, T. (2020). Comprehensive Detection of Very Low Frequency Earthquakes Off the Hokkaido and Tohoku Pacific Coasts, Northeastern Japan. *Journal of Geophysical Research: Solid Earth*, 125(1), 2019JB017988. <https://doi.org/10.1029/2019JB017988>
- Baba, S., Obara, K., Takemura, S., Takeo, A., & Abers, G. A. (2021). Shallow Slow Earthquake Episodes Near the Trench Axis off Costa Rica. *Journal of Geophysical Research: Solid Earth*, 126(9). <https://doi.org/10.1029/2021JB021706>
- Bartlow, N. M., Miyazaki, S., Bradley, A. M., & Segall, P. (2011). Space-time correlation of slip and tremor during the 2009 Cascadia slow slip event. *Geophysical Research Letters*, 38(18), 1–6. <https://doi.org/10.1029/2011GL048714>
- Behr, W. M., & Bürgmann, R. (2021). What’s down there? The structures, materials and environment of deep-seated slow slip and tremor. *Philosophical Transactions of the Royal Society A: Mathematical, Physical and Engineering Sciences*, 379(2193), 20200218. <https://doi.org/10.1098/rsta.2020.0218>
- Beroza, G. C., & Ide, S. (2011). Slow Earthquakes and Nonvolcanic Tremor. *Annual Review of Earth and Planetary Sciences*, 39(1), 271–296. <https://doi.org/10.1146/annurev-earth-040809-152531>

- Beyreuther, M., Barsch, R., Krischer, L., Megies, T., Behr, Y., & Wassermann, J. (2010). ObsPy: A Python Toolbox for Seismology. *Seismological Research Letters*, 81(3), 530–533. <https://doi.org/10.1785/gssrl.81.3.530>
- Brocher, T. M. (2005). Empirical relations between elastic wavespeeds and density in the Earth's crust. *Bulletin of the Seismological Society of America*, 95(6), 2081–2092. <https://doi.org/10.1785/0120050077>
- Brocher, T. M. (2008). Key elements of regional seismic velocity models for long period ground motion simulations. *Journal of Seismology*, 12(2), 217–221. <https://doi.org/10.1007/s10950-007-9061-3>
- Brown, J. R., Beroza, G. C., Ide, S., Ohta, K., Shelly, D. R., Schwartz, S. Y., et al. (2009). Deep low-frequency earthquakes in tremor localize to the plate interface in multiple subduction zones. *Geophysical Research Letters*, 36(19), L19306. <https://doi.org/10.1029/2009GL040027>
- Dixon, T. H., Jiang, Y., Malservisi, R., McCaffrey, R., Voss, N., Protti, M., & Gonzalez, V. (2014). Earthquake and tsunami forecasts: Relation of slow slip events to subsequent earthquake rupture. *Proceedings of the National Academy of Sciences*, 111(48), 17039–17044. <https://doi.org/10.1073/pnas.1412299111>
- Eberhart-Phillips, D., Thurber, C., & Fletcher, J. B. (2014). Imaging P and S Attenuation in the Sacramento-San Joaquin Delta Region, Northern California. *Bulletin of the Seismological Society of America*, 104(5), 2322–2336. <https://doi.org/10.1785/0120130336>
- Fichtner, A., Igel, H., Bunge, H. P., & Kennett, B. L. N. (2009). Simulation and inversion of seismic wave propagation on continental scales based on a spectral-element method. *Journal of Numerical Analysis, Industrial and Applied Mathematics*, 4(1–2), 11–22.
- Goldstein, P., & Snoke, A. (2005). SAC Availability for the IRIS Community. Retrieved from <https://ds.iris.edu/ds/newsletter/vol7/no1/193/sac-availability-for-the-iris-community/>
- Harris, C. R., Millman, K. J., van der Walt, S. J., Gommers, R., Virtanen, P., Cournapeau, D., et al. (2020). Array programming with NumPy. *Nature*, 585(7825), 357–362. <https://doi.org/10.1038/s41586-020-2649-2>
- Herrmann, R. B. (2013). Computer Programs in Seismology: An Evolving Tool for Instruction and Research. *Seismological Research Letters*, 84(6), 1081–1088. <https://doi.org/10.1785/0220110096>
- Ide, S. (2008). A Brownian walk model for slow earthquakes. *Geophysical Research Letters*, 35(17), L17301. <https://doi.org/10.1029/2008GL034821>
- Ide, S. (2016). Characteristics of slow earthquakes in the very low frequency band: Application to the Cascadia subduction zone. *Journal of Geophysical Research: Solid Earth*, 121(8), 5942–5952. <https://doi.org/10.1002/2016JB013085>
- Ide, S. (2021). Empirical Low-Frequency Earthquakes Synthesized From Tectonic Tremor Records. *Journal of Geophysical Research: Solid Earth*, 126(12). <https://doi.org/10.1029/2021JB022498>
- Ide, S., & Beroza, G. C. (2001). Does apparent stress vary with earthquake size? *Geophysical Research Letters*, 28(17), 3349–3352. <https://doi.org/10.1029/2001GL013106>
- Ide, S., & Beroza, G. C. (2023). Slow earthquake scaling reconsidered as a boundary between distinct modes of rupture propagation. *Proceedings of the National Academy of Sciences*, 120(32). <https://doi.org/10.1073/pnas.2222102120>
- Ide, S., & Maury, J. (2018). Seismic Moment, Seismic Energy, and Source Duration of Slow Earthquakes: Application of Brownian slow earthquake model to three major subduction zones. *Geophysical Research Letters*, 45(7), 3059–3067. <https://doi.org/10.1002/2018GL077461>
- Ide, S., & Yabe, S. (2014). Universality of slow earthquakes in the very low frequency band. *Geophysical Research Letters*, 41(8), 2786–2793. <https://doi.org/10.1002/2014GL059712>
- Ide, S., Beroza, G. C., Shelly, D. R., & Uchide, T. (2007). A scaling law for slow earthquakes. *Nature*, 447(7140), 76–79. <https://doi.org/10.1038/nature05780>
- Ide, S., Imanishi, K., Yoshida, Y., Beroza, G. C., & Shelly, D. R. (2008). Bridging the gap between seismically and geodetically detected slow earthquakes. *Geophysical Research Letters*, 35(10), 2–7. <https://doi.org/10.1029/2008GL034014>
- Imperatori, W., & Mai, P. M. (2013). Broad-band near-field ground motion simulations in 3-dimensional scattering media. *Geophysical Journal International*, 192(2), 725–744. <https://doi.org/10.1093/gji/ggs041>
- Ito, Y., Obara, K., Matsuzawa, T., & Maeda, T. (2009). Very low frequency earthquakes related to small asperities on the plate boundary interface at the locked to aseismic transition. *Journal of Geophysical Research: Solid Earth*, 114(B11), 1–16. <https://doi.org/10.1029/2008JB006036>
- Itoh, Y., Aoki, Y., & Fukuda, J. (2022). Imaging evolution of Cascadia slow-slip event using high-rate GPS. *Scientific Reports*, 12(1), 7179. <https://doi.org/10.1038/s41598-022-10957-8>
- Kamei, R., Pratt, R. G., & Tsuji, T. (2012). Waveform tomography imaging of a megasplay fault system in the seismogenic Nankai subduction zone. *Earth and Planetary Science Letters*, 317–318, 343–353. <https://doi.org/10.1016/j.epsl.2011.10.042>

- Kanamori, H., & Rivera, L. (2006). Energy partitioning during an earthquake. *Geophysical Monograph Series*, 170, 3–13. <https://doi.org/10.1029/170GM03>
- Kano, M., Aso, N., Matsuzawa, T., Ide, S., Annoura, S., Arai, R., et al. (2018). Development of a slow earthquake database. *Seismological Research Letters*, 89(4), 1566–1575. <https://doi.org/10.1785/0220180021>
- Kato, A., Obara, K., Igarashi, T., Tsuruoka, H., Nakagawa, S., & Hirata, N. (2012). Propagation of slow slip leading up to the 2011 Mw9.0 Tohoku-Oki earthquake. *Science*, 335(6069), 705–708. <https://doi.org/10.1126/science.1215141>
- Kato, A., Fukuda, J., Kumazawa, T., & Nakagawa, S. (2016). Accelerated nucleation of the 2014 Iquique, Chile Mw 8.2 Earthquake. *Scientific Reports*, 6(1), 24792. <https://doi.org/10.1038/srep24792>
- Koketsu, K., Miyake, H., & Suzuki, H. (2012). Japan Integrated Velocity Structure Model Version 1. *Proceedings of the 15th World Conference on Earthquake Engineering*, 1–4. Retrieved from http://www.iitk.ac.in/nicee/wcee/article/WCEE2012_1773.pdf
- Komatitsch, D., Ritsema, J., & Tromp, J. (2002). Geophysics: The spectral-element method, beowulf computing, and global seismology. *Science*, 298(5599), 1737–1742. <https://doi.org/10.1126/science.1076024>
- Kubo, H., Nakamura, T., Suzuki, W., Kimura, T., Kunugi, T., Takahashi, N., & Aoi, S. (2018). Site Amplification Characteristics at Nankai Seafloor Observation Network, DONET1, Japan, Evaluated Using Spectral Inversion. *Bulletin of the Seismological Society of America*, XX(Xx), 1–9. <https://doi.org/10.1785/0120170254>
- Kubo, H., Nakamura, T., Suzuki, W., Kunugi, T., Takahashi, N., & Aoi, S. (2020). Site characteristics of DONET1 seafloor observation network, Japan, evaluated by HVRS of coda and ambient noise. In *Proceedings of the 17th World Conference on Earthquake Engineering*. Sendai, Japan.
- Maeda, T., Takemura, S., & Furumura, T. (2017). OpenSWPC: An open-source integrated parallel simulation code for modeling seismic wave propagation in 3D heterogeneous viscoelastic media 4. *Seismology, Earth, Planets and Space*, 69(1). <https://doi.org/10.1186/s40623-017-0687-2>
- Maury, J., Ide, S., Cruz-Atienza, V. M., Kostoglodov, V., González-Molina, G., & Pérez-Campos, X. (2016). Comparative study of tectonic tremor locations: Characterization of slow earthquakes in Guerrero, Mexico. *Journal of Geophysical Research: Solid Earth*, 121(7), 5136–5151. <https://doi.org/10.1002/2016JB013027>
- Maury, J., Ide, S., Cruz-Atienza, V. M., & Kostoglodov, V. (2018). Spatiotemporal Variations in Slow Earthquakes Along the Mexican Subduction Zone. *Journal of Geophysical Research: Solid Earth*, 123(2), 1559–1575. <https://doi.org/10.1002/2017JB014690>
- Morioka, H., Kumagai, H., & Maeda, T. (2017). Theoretical basis of the amplitude source location method for volcano-seismic signals. *Journal of Geophysical Research: Solid Earth*, 122(8), 6538–6551. <https://doi.org/10.1002/2017JB013997>
- Nakano, Masara, Nakamura, T., Kamiya, S., Ohori, M., & Kaneda, Y. (2013). Intensive seismic activity around the Nankai trough revealed by DONET ocean-floor seismic observations. *Earth, Planets and Space*, 65(1), 5–15. <https://doi.org/10.5047/eps.2012.05.013>
- Nakano, Masaru, Hori, T., Araki, E., Kodaira, S., & Ide, S. (2018). Shallow very-low-frequency earthquakes accompany slow slip events in the Nankai subduction zone. *Nature Communications*, 9(1), 984. <https://doi.org/10.1038/s41467-018-03431-5>
- Nakano, Masaru, Yabe, S., Sugioka, H., Shinohara, M., & Ide, S. (2019). Event Size Distribution of Shallow Tectonic Tremor in the Nankai Trough. *Geophysical Research Letters*, 46(11), 5828–5836. <https://doi.org/10.1029/2019GL083029>
- National Research Institute for Earth Science and Disaster Resilience. (2019a). NIED DONET. <https://doi.org/10.17598/NIED.0008>
- National Research Institute for Earth Science and Disaster Resilience. (2019b). NIED F-net. <https://doi.org/10.17598/NIED.0005>
- National Research Institute for Earth Science and Disaster Resilience. (2019c). NIED Hi-net. <https://doi.org/10.17598/NIED.0003>
- National Research Institute for Earth Science and Disaster Resilience. (2019d). NIED S-net. <https://doi.org/10.17598/NIED.0007>
- Nishikawa, T., Matsuzawa, T., Ohta, K., Uchida, N., Nishimura, T., & Ide, S. (2019). The slow earthquake spectrum in the Japan Trench illuminated by the S-net seafloor observatories. *Science*, 365(August), 808–813. <https://doi.org/10.1126/science.aax5618>
- Nishikawa, Tomoaki, Ide, S., & Nishimura, T. (2023). A review on slow earthquakes in the Japan Trench. *Progress in Earth and Planetary Science*, 10(1), 1. <https://doi.org/10.1186/s40645-022-00528-w>
- Obara, K. (2020). Characteristic activities of slow earthquakes in Japan. *Proceedings of the Japan Academy Series B: Physical and Biological Sciences*, 96(7), 297–315. <https://doi.org/10.2183/PJAB.96.022>

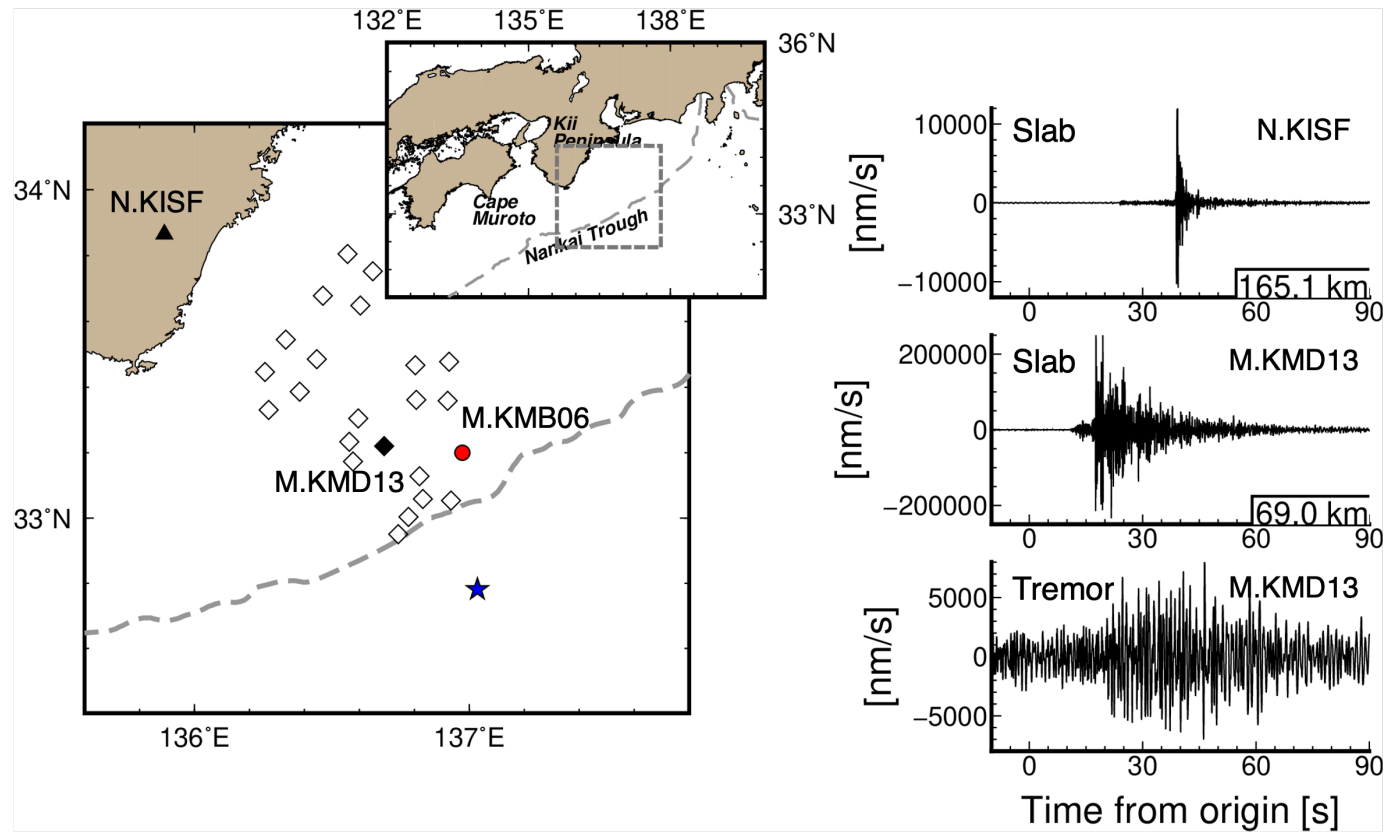
- Obara, K., & Kato, A. (2016). Connecting slow earthquakes to huge earthquakes. *Science*, 353(6296), 253–257. <https://doi.org/10.1126/science.aaf1512>
- Obara, K., Hirose, H., Yamamizu, F., & Kasahara, K. (2004). Episodic slow slip events accompanied by non-volcanic tremors in southwest Japan subduction zone. *Geophysical Research Letters*, 31(23). <https://doi.org/10.1029/2004GL020848>
- Plata-Martinez, R., Ide, S., Shinohara, M., Garcia, E. S., Mizuno, N., Dominguez, L. A., et al. (2021). Shallow slow earthquakes to decipher future catastrophic earthquakes in the Guerrero seismic gap. *Nature Communications*, 12(1), 3976. <https://doi.org/10.1038/s41467-021-24210-9>
- Rogers, G., & Dragert, H. (2003). Episodic tremor and slip on the Cascadia subduction zone: the chatter of silent slip. *Science*, 300(5627), 1942–1943. <https://doi.org/10.1126/science.1084783>
- Saffer, D. M., & Wallace, L. M. (2015). The frictional, hydrologic, metamorphic and thermal habitat of shallow slow earthquakes. *Nature Geoscience*, 8(8), 594–600. <https://doi.org/10.1038/ngeo2490>
- Sato, H., Fehler, M. C., & Maeda, T. (2012). *Seismic Wave Propagation and Scattering in the Heterogeneous Earth : Second Edition*. Berlin, Heidelberg: Springer Berlin Heidelberg. https://doi.org/10.1007/978-3-642-23029-5_2
- Schwartz, S. Y., & Rokosky, J. M. (2007). Slow slip events and seismic tremor at circum-Pacific subduction zones. *Reviews of Geophysics*, 45(3). <https://doi.org/10.1029/2006RG000208>
- Shelly, D. R., Beroza, G. C., & Ide, S. (2007). Non-volcanic tremor and low-frequency earthquake swarms. *Nature*, 446(7133), 305–307. <https://doi.org/10.1038/nature05666>
- Sugioka, H., Okamoto, T., Nakamura, T., Ishihara, Y., Ito, A., Obana, K., et al. (2012). Tsunamigenic potential of the shallow subduction plate boundary inferred from slow seismic slip. *Nature Geoscience*, 5(6), 414–418. <https://doi.org/10.1038/ngeo1466>
- Syracuse, E. M., van Keken, P. E., Abers, G. A., Suetsugu, D., Bina, C., Inoue, T., et al. (2010). The global range of subduction zone thermal models. *Physics of the Earth and Planetary Interiors*, 183(1–2), 73–90. <https://doi.org/10.1016/j.pepi.2010.02.004>
- Takemoto, T., Furumura, T., Saito, T., Maeda, T., & Noguchi, S. (2012). Spatial- and frequency-dependent properties of site amplification factors in Japan derived by the coda normalization method. *Bulletin of the Seismological Society of America*, 102(4), 1462–1476. <https://doi.org/10.1785/0120110188>
- Takemura, S., Furumura, T., & Saito, T. (2009). Distortion of the apparent *S*-wave radiation pattern in the high-frequency wavefield: Tottori-Ken Seibu, Japan, earthquake of 2000. *Geophysical Journal International*, 178(2), 950–961. <https://doi.org/10.1111/j.1365-246X.2009.04210.x>
- Takemura, Shunsuke. (2023). Estimated site amplifications at DONET stations, 1D velocity models, and movies for seismic wave propagation in a local 1D models [Data set]. <https://doi.org/10.5281/zenodo.10030902>
- Takemura, Shunsuke, Kobayashi, M., & Yoshimoto, K. (2016). Prediction of maximum P- and S-wave amplitude distributions incorporating frequency- and distance-dependent characteristics of the observed apparent radiation patterns. *Earth, Planets and Space*, 68(1), 166. <https://doi.org/10.1186/s40623-016-0544-8>
- Takemura, Shunsuke, Matsuzawa, T., Noda, A., Tonegawa, T., Asano, Y., Kimura, T., & Shiomi, K. (2019). Structural Characteristics of the Nankai Trough Shallow Plate Boundary Inferred From Shallow Very Low Frequency Earthquakes. *Geophysical Research Letters*, 46(8), 4192–4201. <https://doi.org/10.1029/2019GL082448>
- Takemura, Shunsuke, Okuwaki, R., Kubota, T., Shiomi, K., Kimura, T., & Noda, A. (2020). Centroid moment tensor inversions of offshore earthquakes using a three-dimensional velocity structure model: slip distributions on the plate boundary along the Nankai Trough. *Geophysical Journal International*, 222(2), 1109–1125. <https://doi.org/10.1093/gji/ggaa238>
- Takemura, Shunsuke, Yabe, S., & Emoto, K. (2020). Modelling high-frequency seismograms at ocean bottom seismometers: effects of heterogeneous structures on source parameter estimation for small offshore earthquakes and shallow low-frequency tremors. *Geophysical Journal International*, 223(3), 1708–1723. <https://doi.org/10.1093/gji/ggaa404>
- Takemura, Shunsuke, Yoshimoto, K., & Shiomi, K. (2021). Long-period ground motion simulation using centroid moment tensor inversion solutions based on the regional three-dimensional model in the Kanto region, Japan. *Earth, Planets and Space*, 73(1), 15. <https://doi.org/10.1186/s40623-020-01348-2>
- Takemura, Shunsuke, Baba, S., Yabe, S., Yamashita, Y., Shiomi, K., & Matsuzawa, T. (2022). Detectability analysis of very low frequency earthquakes: Methods and application in Nankai using F-net and DONET broadband seismometers. *Research Square*. Retrieved from <https://doi.org/10.21203/rs.3.rs-2351814/v1>
- Takemura, Shunsuke, Baba, S., Yabe, S., Emoto, K., Shiomi, K., & Matsuzawa, T. (2022). Source Characteristics and Along-Strike Variations of Shallow Very Low Frequency Earthquake Swarms on the Nankai Trough

- Shallow Plate Boundary. *Geophysical Research Letters*, 49(11), e2022GL097979.
<https://doi.org/10.1029/2022GL097979>
- Takemura, Shunsuke, Obara, K., Shiomi, K., & Baba, S. (2022). Spatiotemporal Variations of Shallow Very Low Frequency Earthquake Activity Southeast Off the Kii Peninsula, Along the Nankai Trough, Japan. *Journal of Geophysical Research: Solid Earth*, 127(3), e2021JB023073. <https://doi.org/10.1029/2021JB023073>
- Takemura, Shunsuke, Hamada, Y., Okuda, H., Okada, Y., Okubo, K., Akuhara, T., et al. (2023). A review of shallow slow earthquakes along the Nankai Trough. *Earth, Planets and Space*, 75(1), 164.
<https://doi.org/10.1186/s40623-023-01920-6>
- Takemura, Shunsuke, Emoto, K., & Yamaya, L. (2023). High-frequency S and S-coda waves at ocean-bottom seismometers. *Earth, Planets and Space*, 75(1), 20. <https://doi.org/10.1186/s40623-023-01778-8>
- Takeo, A., Idehara, K., Iritani, R., Tonegawa, T., Nagaoka, Y., Nishida, K., et al. (2010). Very broadband analysis of a swarm of very low frequency earthquakes and tremors beneath Kii Peninsula, SW Japan. *Geophysical Research Letters*, 37(6), L06311. <https://doi.org/10.1029/2010GL042586>
- Tamaribuchi, K., Ogiso, M., & Noda, A. (2022). Spatiotemporal Distribution of Shallow Tremors along the Nankai Trough, Southwest Japan, as Determined from Waveform Amplitudes and Cross-Correlations. *Journal of Geophysical Research: Solid Earth*. <https://doi.org/10.1029/2022JB024403>
- Tian, D. (2020). HinetPy: A Python package to request and process seismic waveform data from Hi-net. <https://doi.org/10.5281/zenodo.3885779>
- Todd, E. K., Schwartz, S. Y., Mochizuki, K., Wallace, L. M., Sheehan, A. F., Webb, S. C., et al. (2018). Earthquakes and Tremor Linked to Seamount Subduction During Shallow Slow Slip at the Hikurangi Margin, New Zealand. *Journal of Geophysical Research: Solid Earth*. <https://doi.org/10.1029/2018JB016136>
- Toh, A., Capdeville, Y., Chi, W. -C., & Ide, S. (2023). Strongly Scattering Medium Along Slow Earthquake Fault Zones Based on New Observations of Short-Duration Tremors. *Geophysical Research Letters*, 50(8).
<https://doi.org/10.1029/2022GL101851>
- Tonegawa, T., Araki, E., Kimura, T., Nakamura, T., Nakano, M., & Suzuki, K. (2017). Sporadic low-velocity volumes spatially correlate with shallow very low frequency earthquake clusters. *Nature Communications*, 8(1), 2048. <https://doi.org/10.1038/s41467-017-02276-8>
- Trugman, D. T., Chu, S. X., & Tsai, V. C. (2021). Earthquake Source Complexity Controls the Frequency Dependence of Near-Source Radiation Patterns. *Geophysical Research Letters*, 48(17).
<https://doi.org/10.1029/2021GL095022>
- Vaca, S., Vallée, M., Nocquet, J. M., Battaglia, J., & Régnier, M. (2018). Recurrent slow slip events as a barrier to the northward rupture propagation of the 2016 Pedernales earthquake (Central Ecuador). *Tectonophysics*, 724–725(November 2017), 80–92. <https://doi.org/10.1016/j.tecto.2017.12.012>
- Virtanen, P., Gommers, R., Oliphant, T. E., Haberland, M., Reddy, T., Cournapeau, D., et al. (2020). SciPy 1.0: fundamental algorithms for scientific computing in Python. *Nature Methods*, 17(3), 261–272.
<https://doi.org/10.1038/s41592-019-0686-2>
- Voss, N., Dixon, T. H., Liu, Z., Malservisi, R., Protti, M., & Schwartz, S. (2018). Do slow slip events trigger large and great megathrust earthquakes ? *Science Advances*, 4(10), eaat8472.
- Walter, J. I., Schwartz, S. Y., Protti, M., & Gonzalez, V. (2013). The synchronous occurrence of shallow tremor and very low frequency earthquakes offshore of the Nicoya Peninsula, Costa Rica. *Geophysical Research Letters*, 40(8), 1517–1522. <https://doi.org/10.1002/grl.50213>
- Wech, A. G. (2021). Cataloging Tectonic Tremor Energy Radiation in the Cascadia Subduction Zone. *Journal of Geophysical Research: Solid Earth*, 126(10). <https://doi.org/10.1029/2021JB022523>
- Wessel, P., Smith, W. H. F., Scharroo, R., Luis, J., & Wobbe, F. (2013). Generic mapping tools: Improved version released. *Eos*, 94(45), 409–410. <https://doi.org/10.1002/2013EO450001>
- Yabe, S., & Ide, S. (2014). Spatial distribution of seismic energy rate of tectonic tremors in subduction zones. *Journal of Geophysical Research: Solid Earth*, 119(11), 8171–8185. <https://doi.org/10.1002/2014JB011383>
- Yabe, S., Tonegawa, T., & Nakano, M. (2019). Scaled Energy Estimation for Shallow Slow Earthquakes. *Journal of Geophysical Research: Solid Earth*, 124(2), 1507–1519. <https://doi.org/10.1029/2018JB016815>
- Yabe, S., Baba, S., Tonegawa, T., Nakano, M., & Takemura, S. (2021). Seismic energy radiation and along-strike heterogeneities of shallow tectonic tremors at the Nankai Trough and Japan Trench. *Tectonophysics*, 800, 228714. <https://doi.org/10.1016/j.tecto.2020.228714>
- Yamamoto, Y., Ariyoshi, K., Yada, S., Nakano, M., & Hori, T. (2022). Spatio-temporal distribution of shallow very-low-frequency earthquakes between December 2020 and January 2021 in Kumano-nada, Nankai subduction zone, detected by a permanent seafloor seismic network. *Earth, Planets and Space*, 74(1), 14.
<https://doi.org/10.1186/s40623-022-01573-x>

921 Yoshida, K., Emoto, K., Takemura, S., & Matsuzawa, T. (2023). Near-Source Waveform Modeling to Estimate
922 Shallow Crustal Attenuation and Radiated Energy of Mw 2.0-4.5 Earthquakes. *ESS Open Archive*.
923 <https://doi.org/10.22541/essoar.170326156.62618173/v1>
924

Figure 1.

(a)



(b)

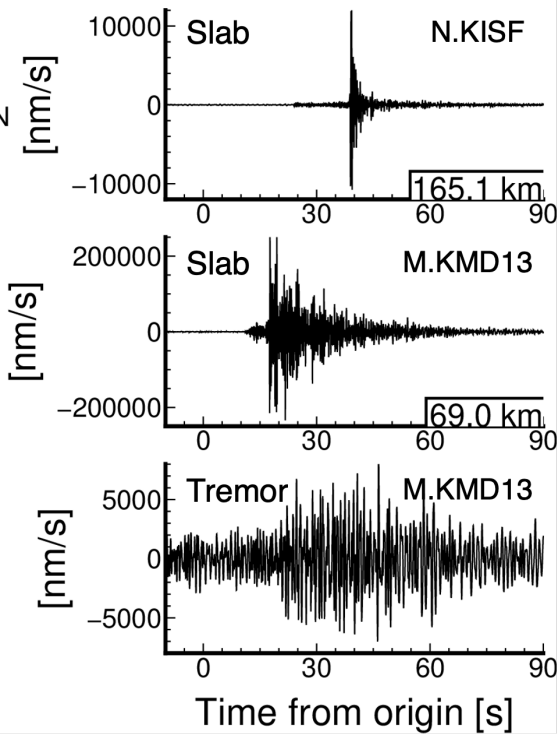
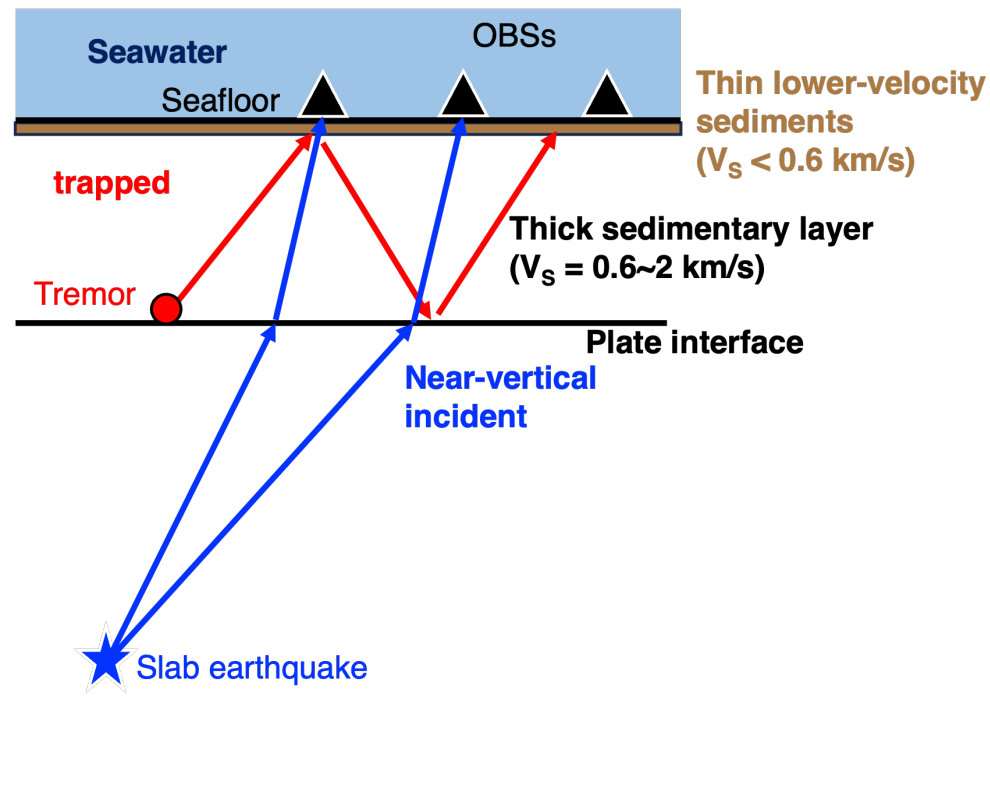
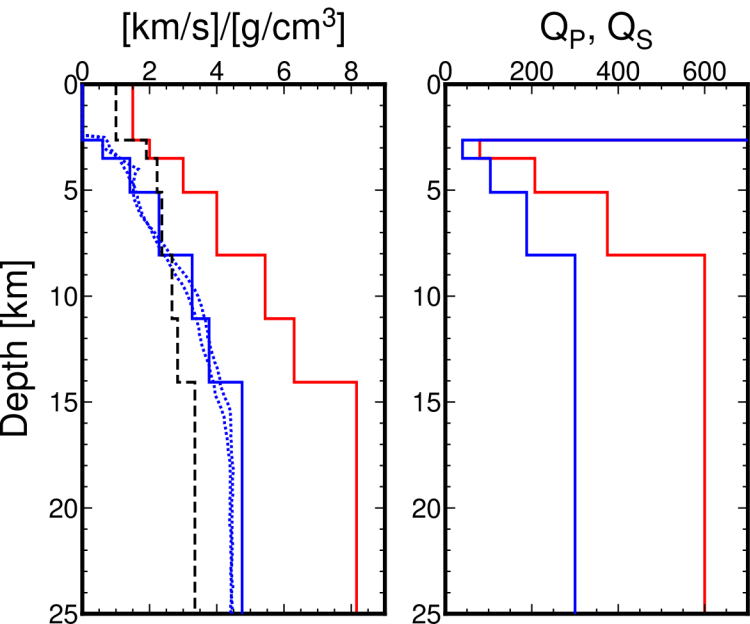


Figure 2.

(a) DONET1D



(b) DONET1D'

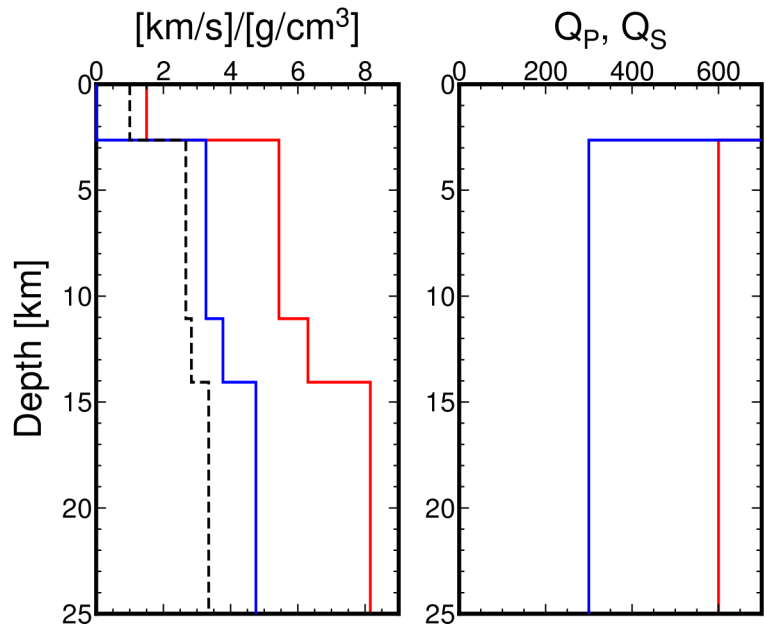


Figure 3.

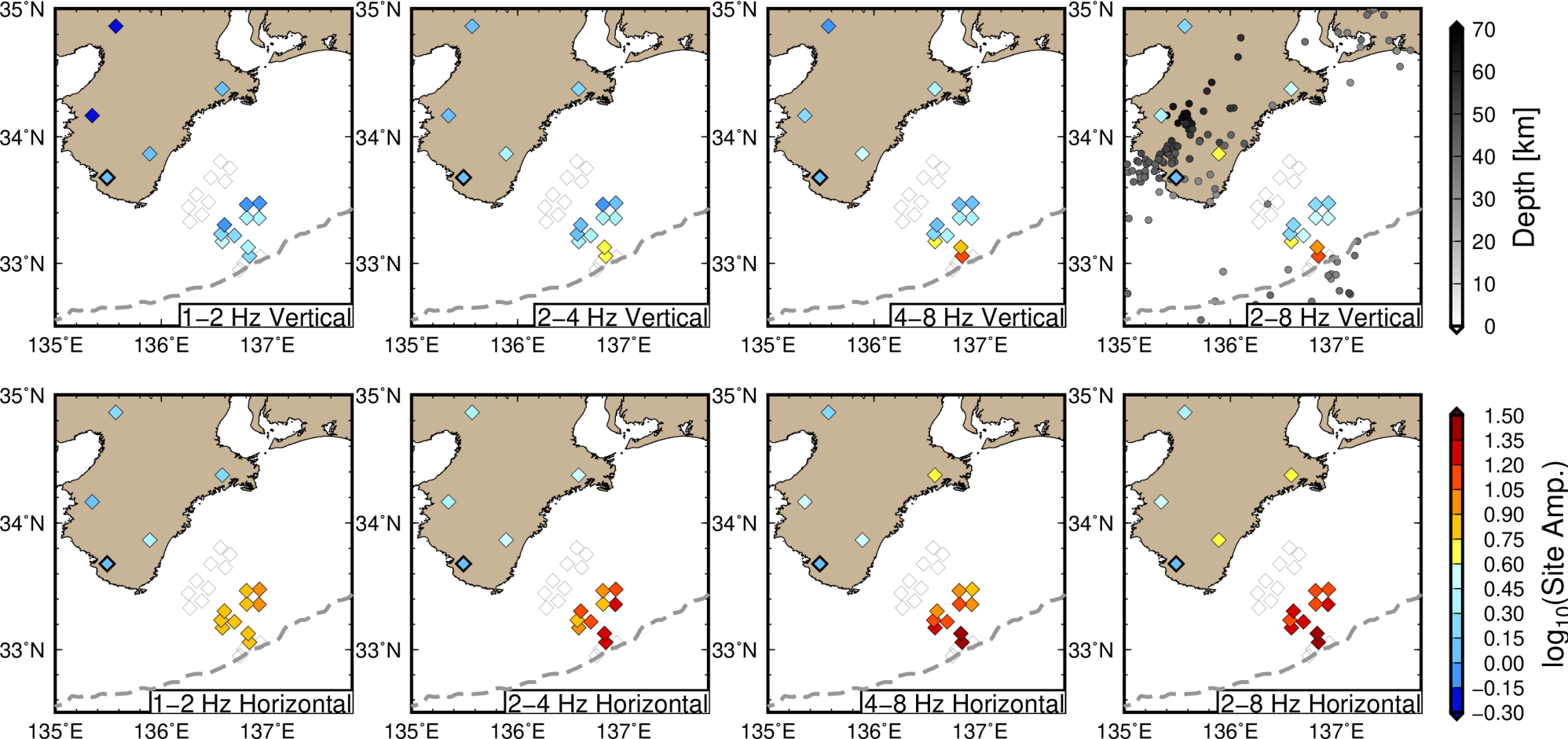


Figure 4.

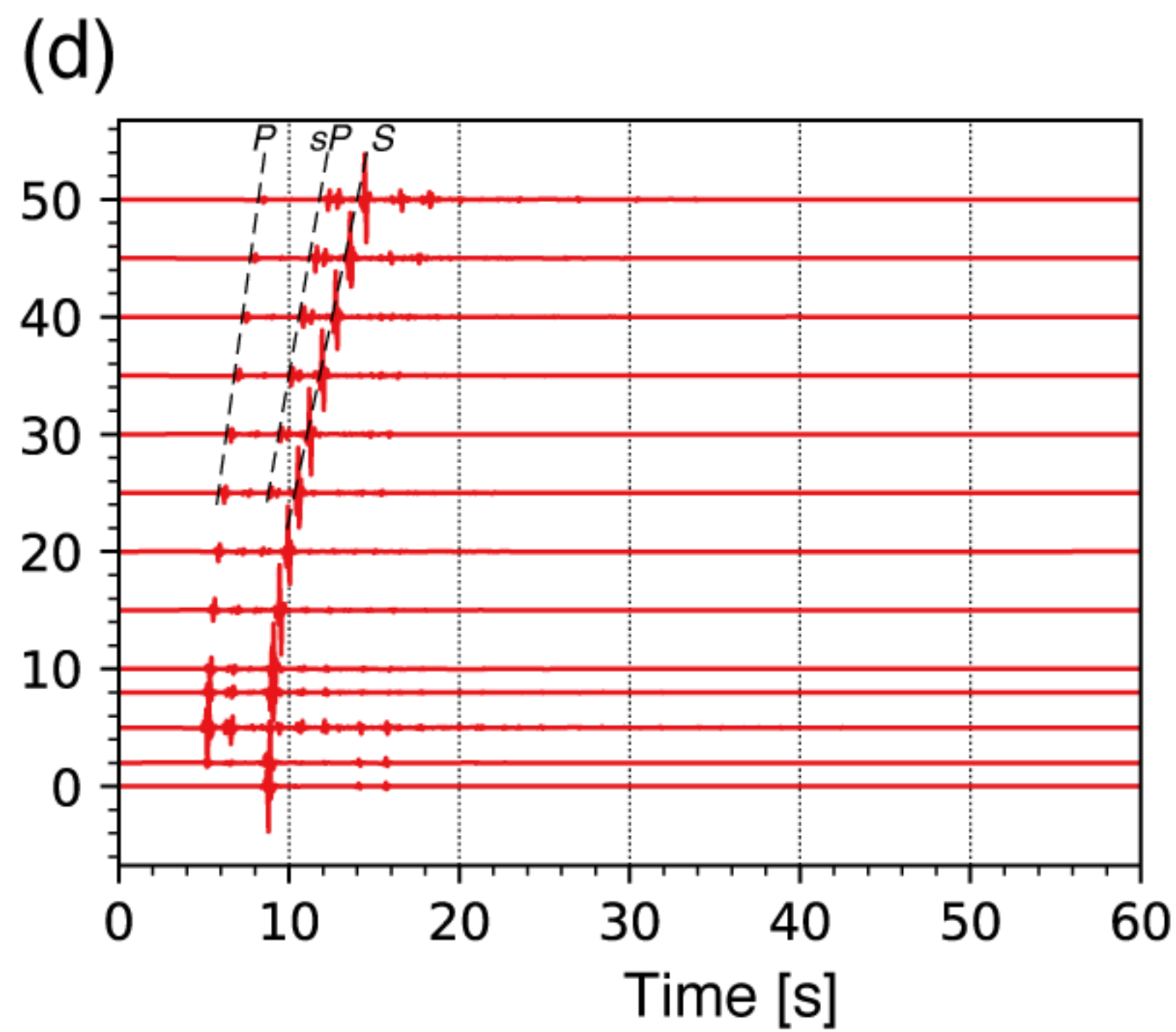
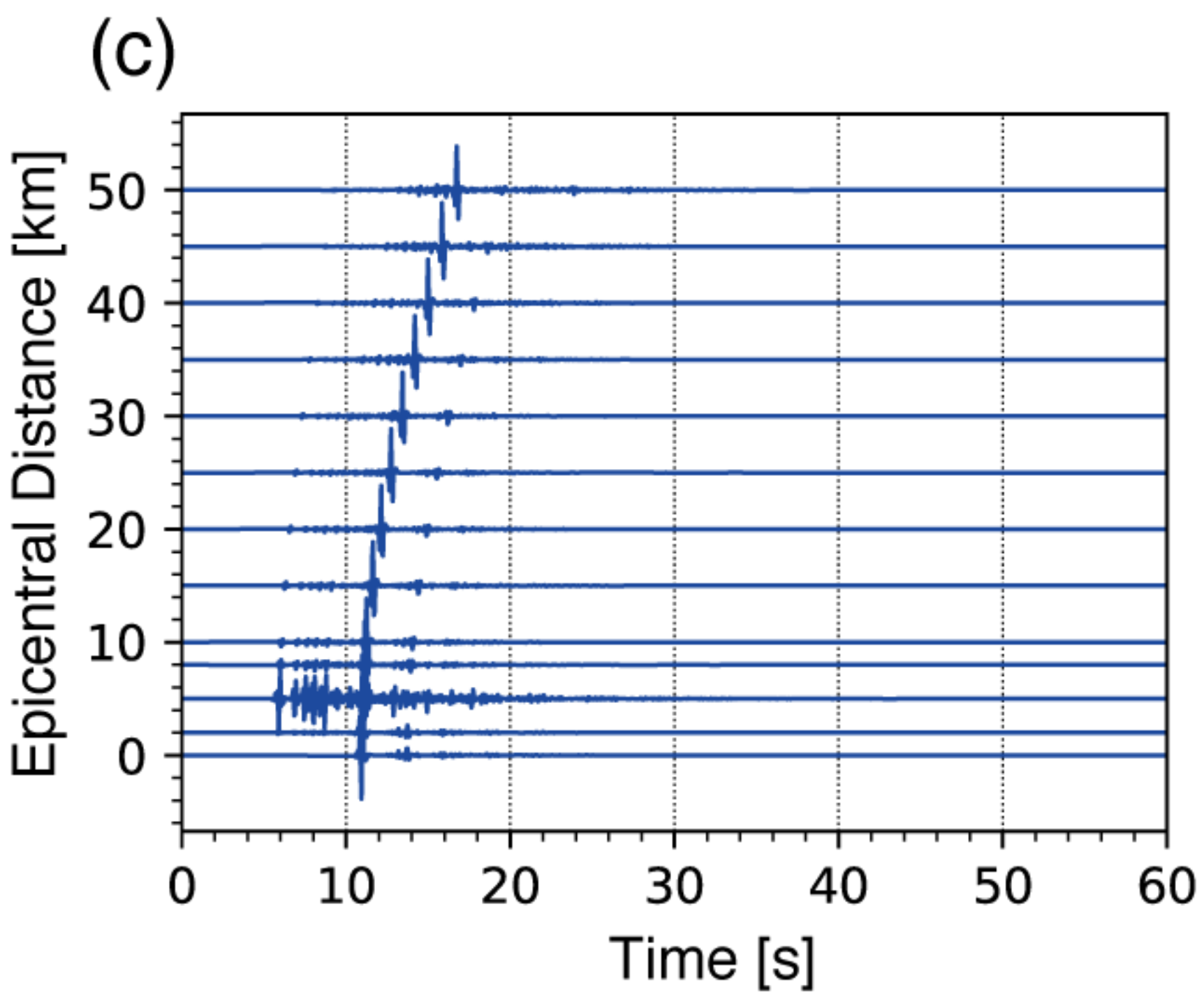
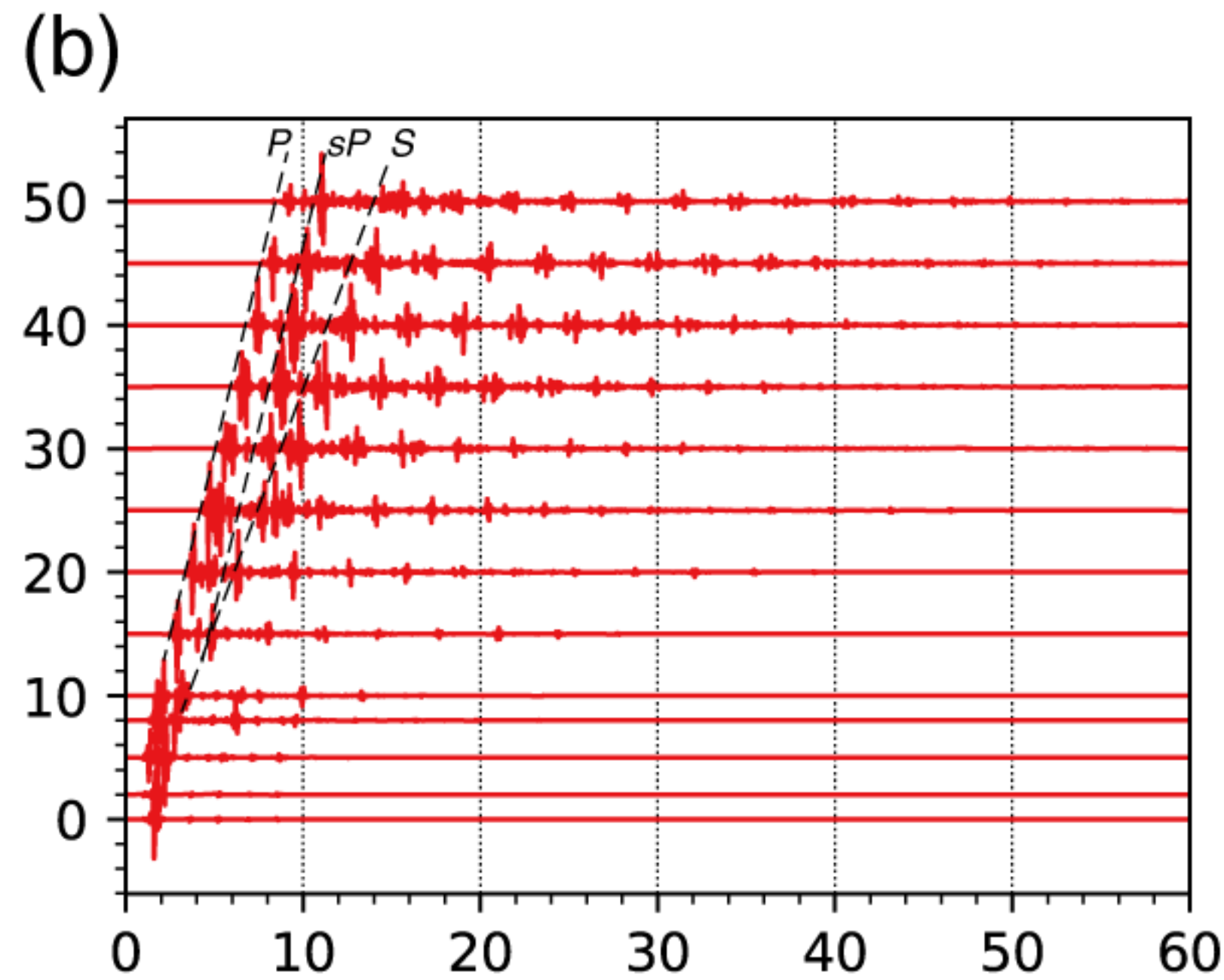
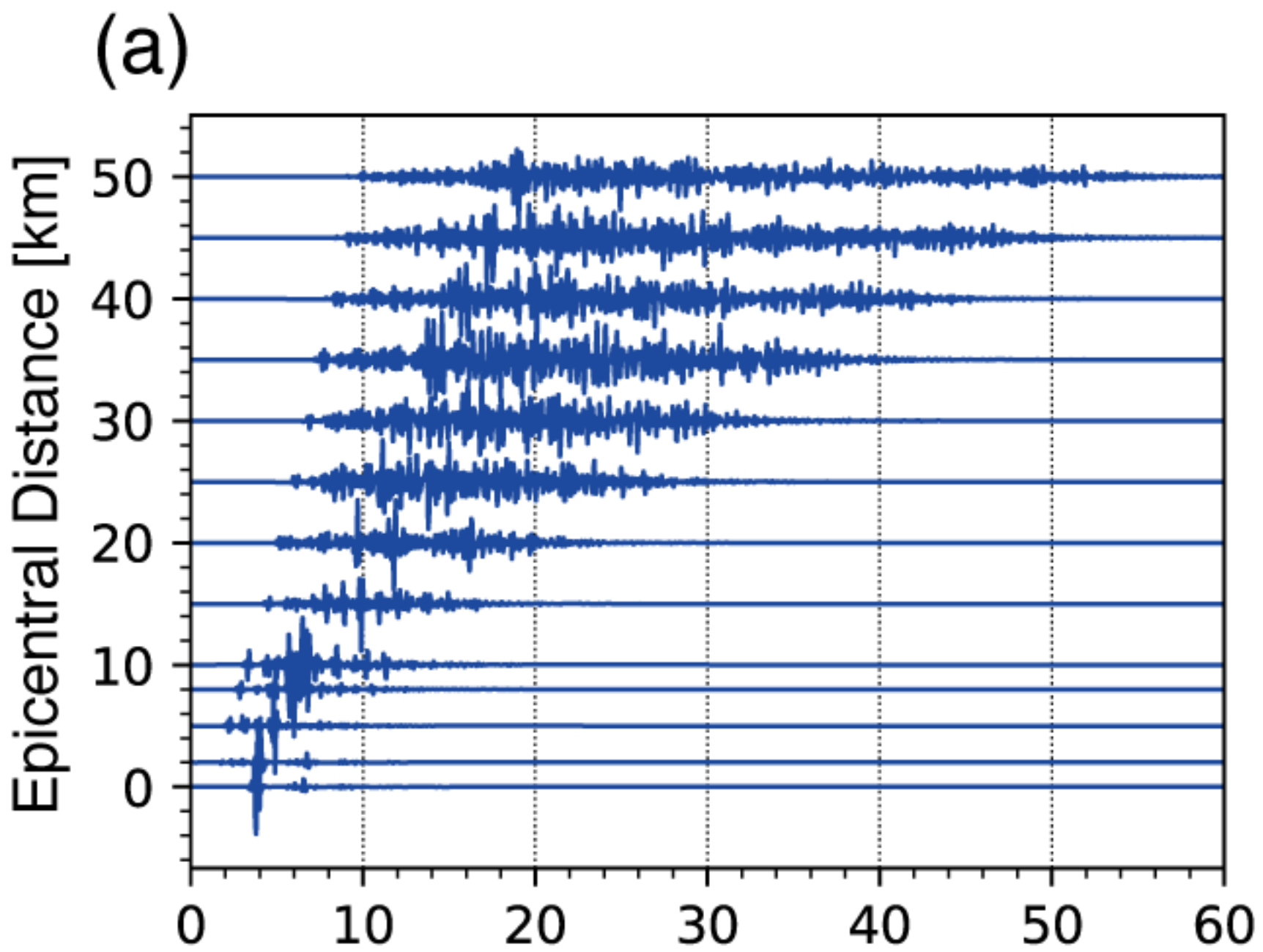


Figure 5.

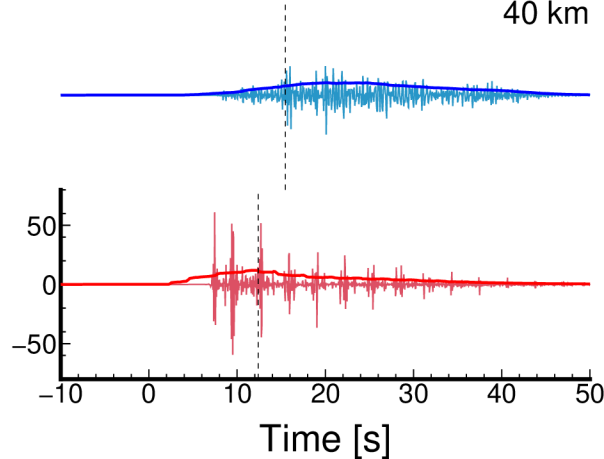
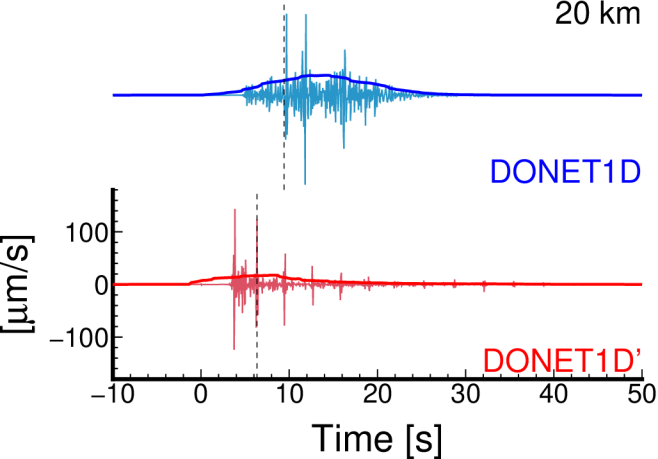


Figure 6.

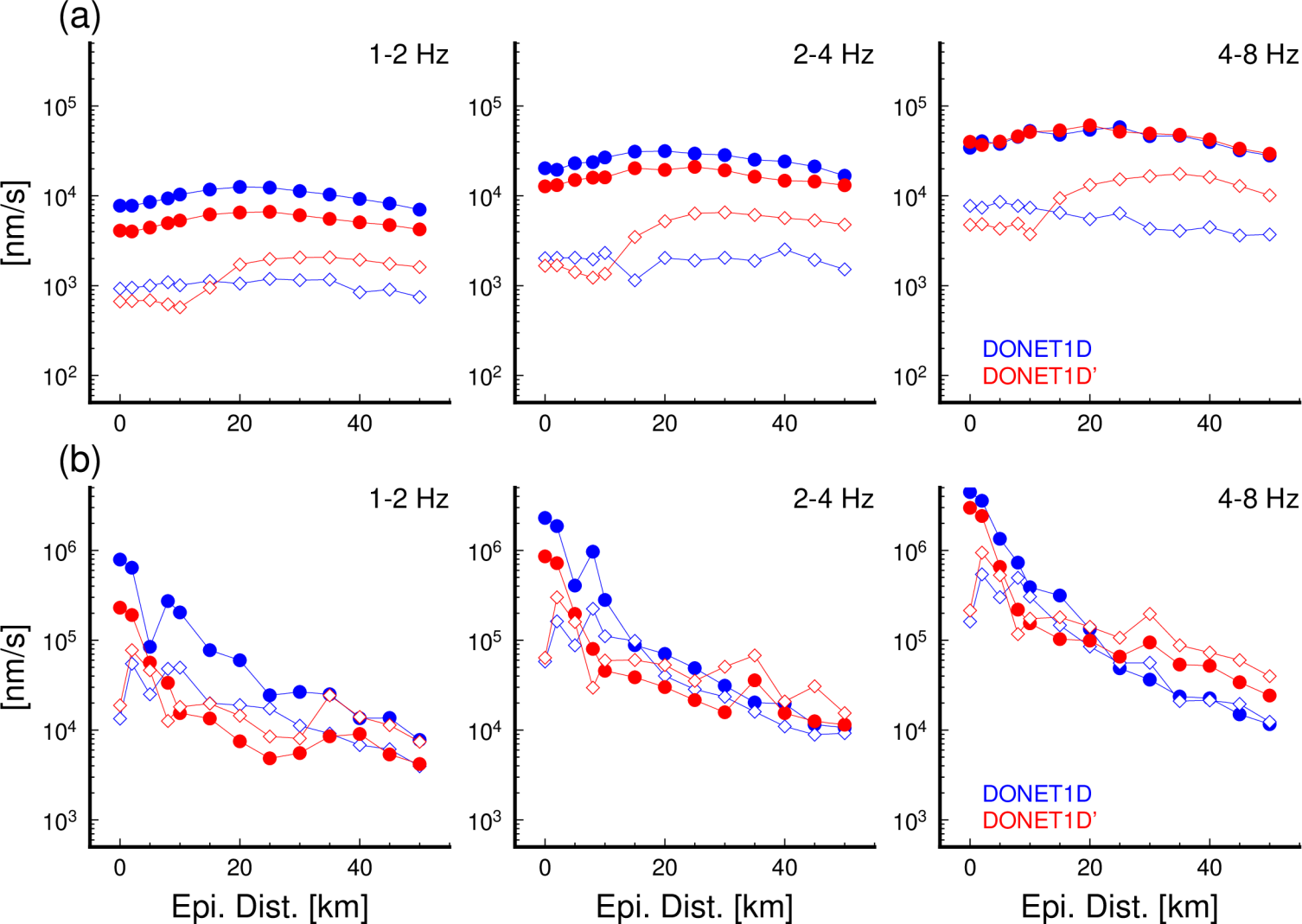
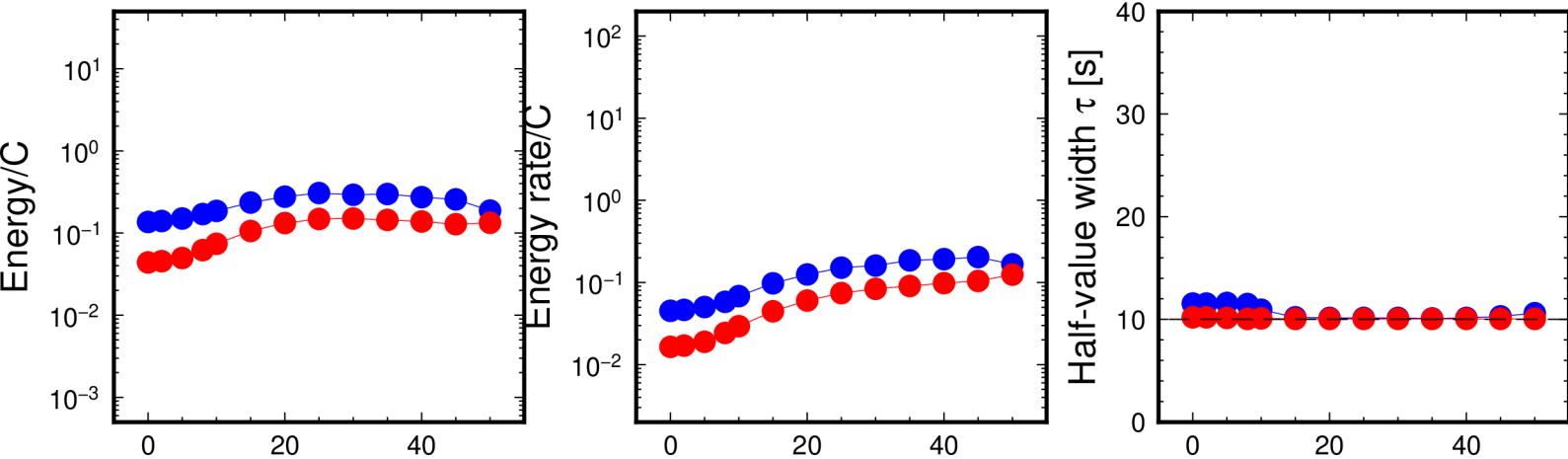


Figure 7.

(a)



(b)

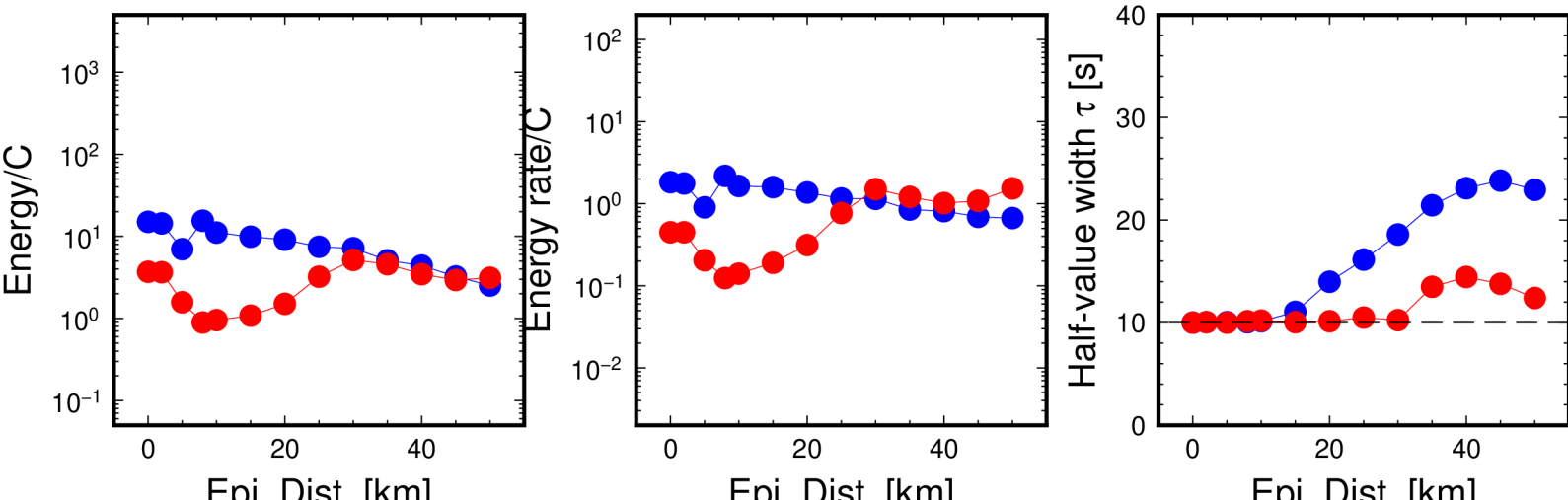


Figure 8.

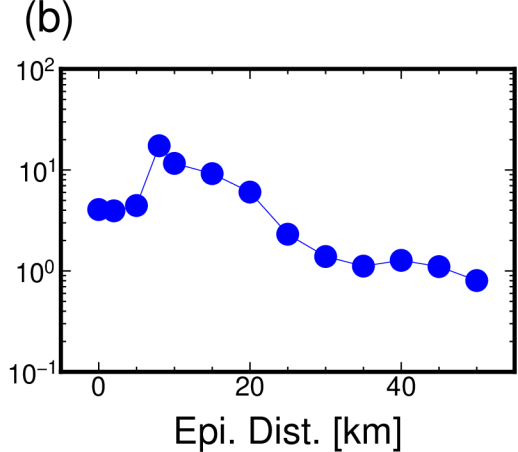
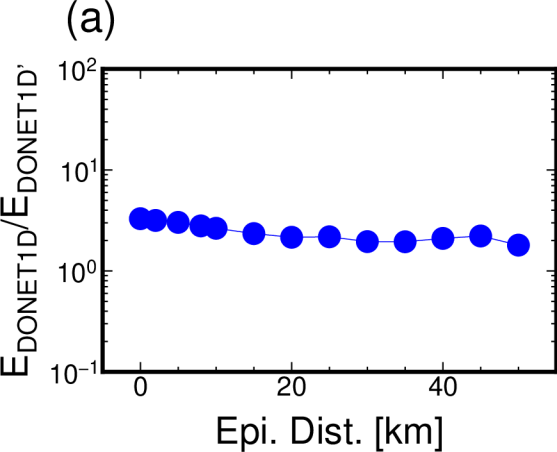


Figure 9.

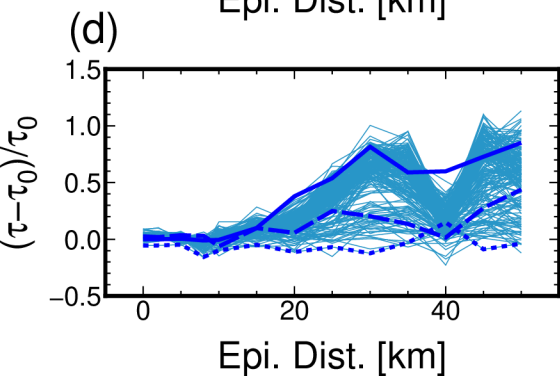
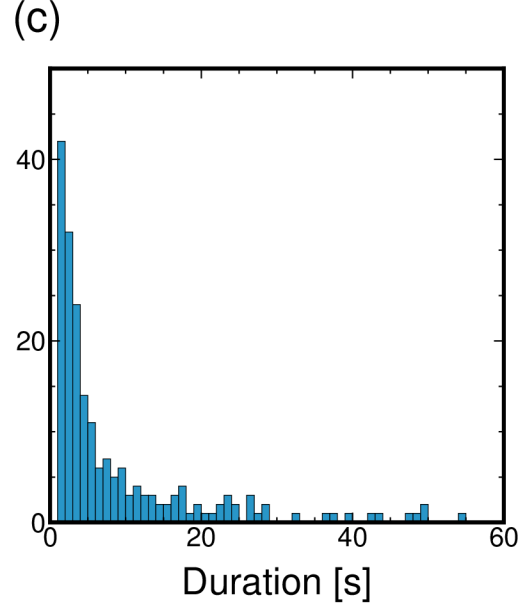
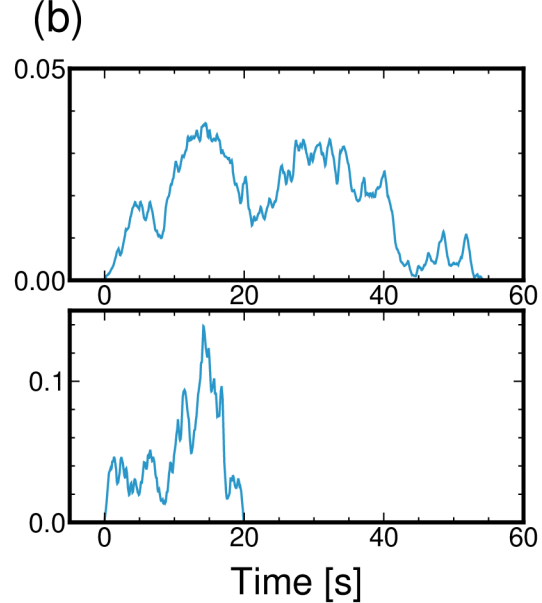
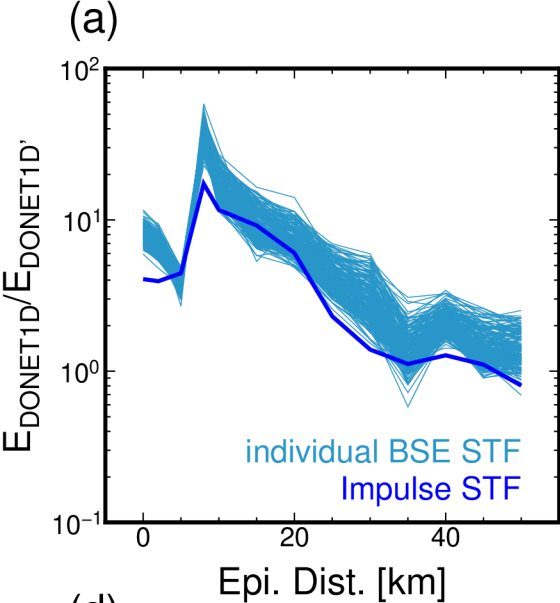


Figure 10.

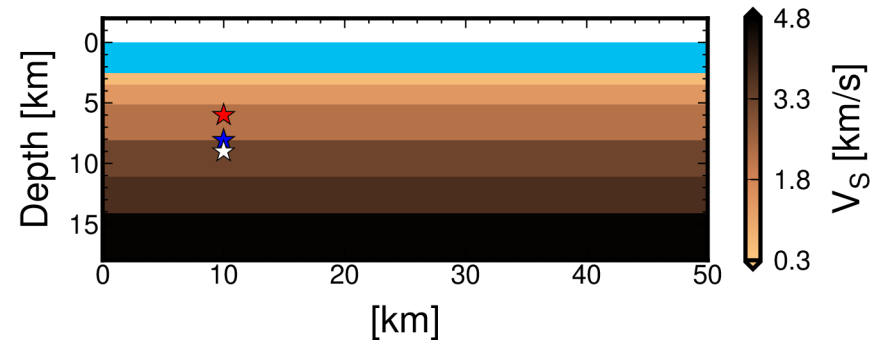
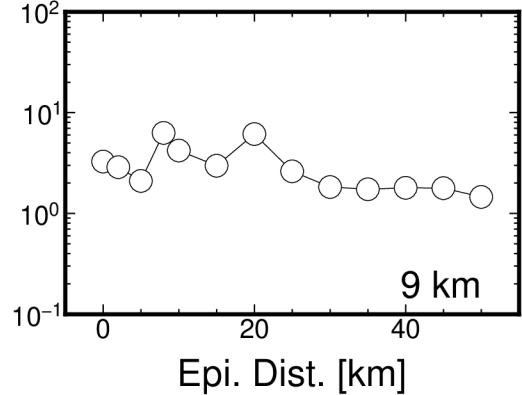
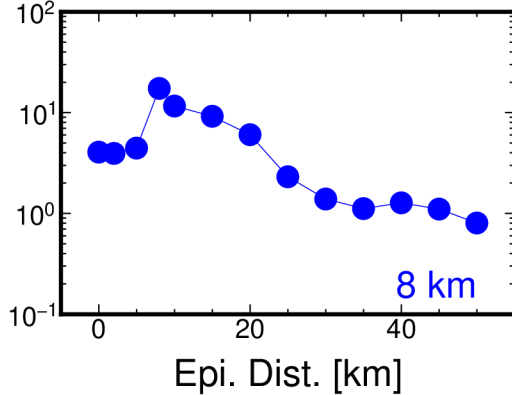
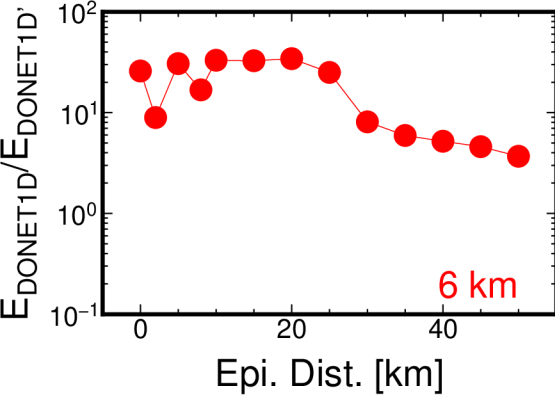


Figure 11.

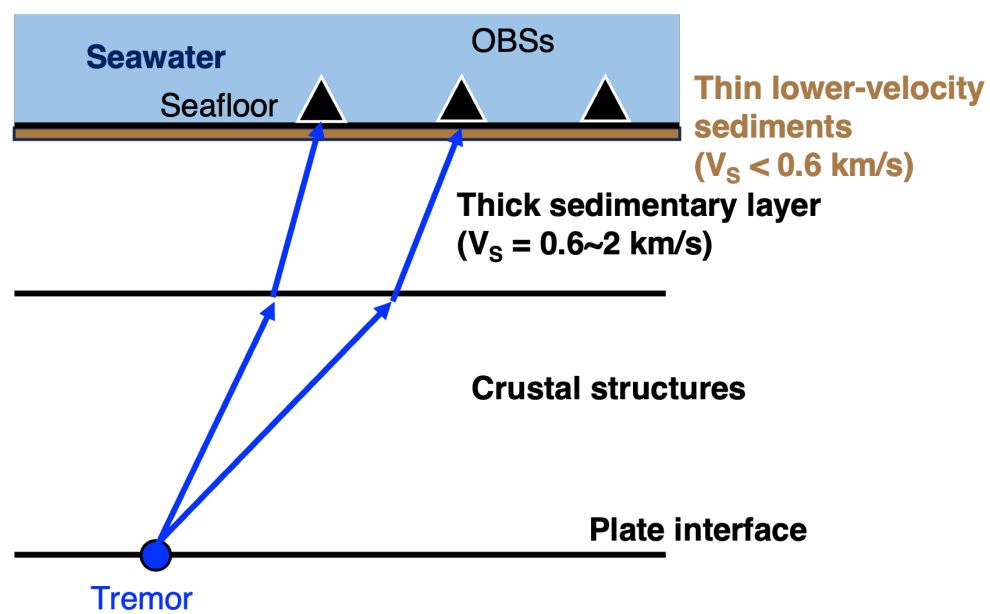
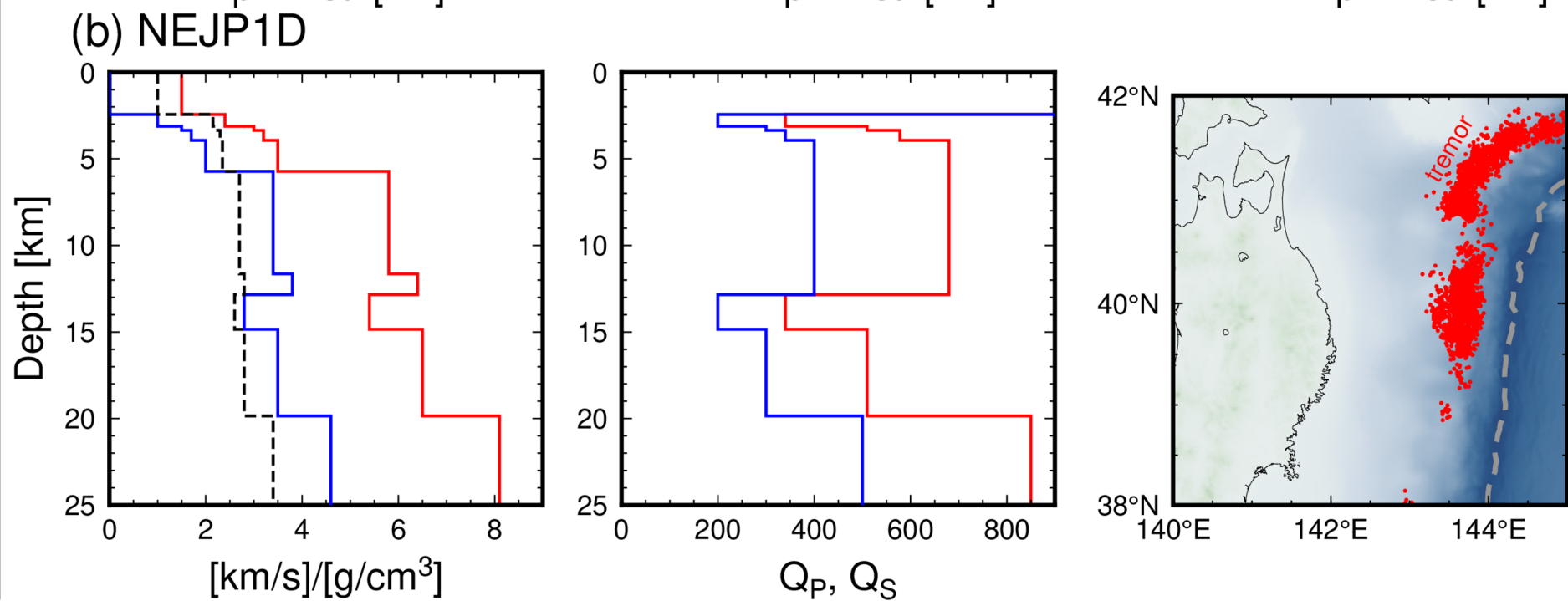
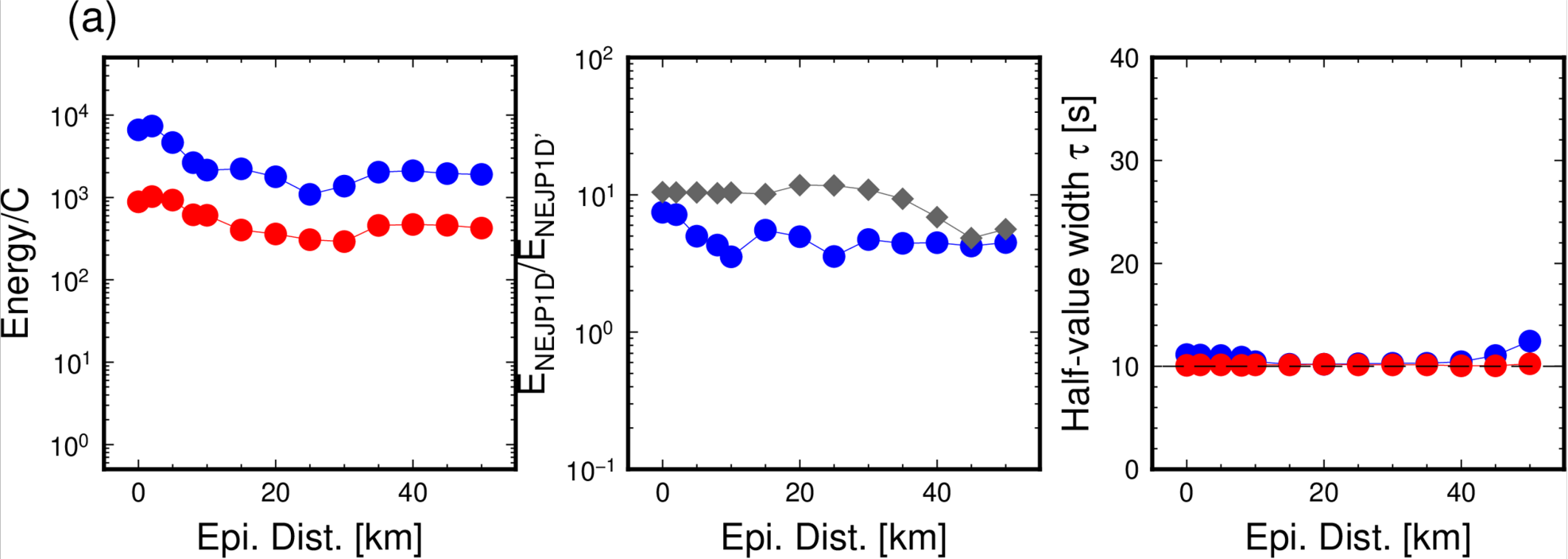


Figure 12.

